Unraveling the influence of Mo on the corrosion mechanism of Ni-advanced weathering steel in harsh marine atmospheric environments

Gang Niu [a 1], Rui Yuan [a c 1], Enmao Wang [a 1], Xiaojia Yang [a], Zhiying Liu [b], Zhangyin Li [c], Zhihui Zhang [a], Na Gong [d], Kun Li [e], Baoxian Su [f], Junhua Zhang [c], Huibin Wu [a], Xiaogang Li [a], Lawrence E. Murr [g]

[a] Collaborative Innovation Center of Steel Technology, University of Science and Technology Beijing, Beijing 100083, China

[b] Max-Planck-Institut für Eisenforschung GmbH, Max-Planck-Str. 1, D-40237 Düsseldorf, Germany

[c] Engineering Technology Research Institute, Chery Automobile Co., Ltd., Wuhu 241006, China

[d] Institute of Materials Research and Engineering (IMRE), Agency for Science, Technology and Research (A*STAR), 2 Fusionopolis Way, Innovis #08-03, Singapore 138634, Republic of Singapore

[e] College of Mechanical and Vehicle Engineering, Chongqing University, Chongqing 400044, China

[f] National Key Laboratory for Precision Hot Processing of Metals, School of Materials Science and Engineering, Harbin Institute of Technology, Harbin 150001, China

[g] Department of Metallurgical, Materials and Biomedical Engineering, University of Texas at El Paso, El Paso, TX 79968, USA

Abstract

Ni-advanced weathering steel holds paramount importance in marine atmospheric environments, especially those with heightened Cl^- concentrations. The meticulous compositional design plays a crucial role in establishing a rust layer capable of withstanding intrusion by Cl^-, making it imperative for the viability of coating-free weathering steel in marine atmospheric environments. This study explores the corrosion evolution and corrosion-resistant mechanisms within a steady-state rust layer in 3Ni weathering steel, with a particular focus on the role of Mo in challenging marine atmospheric conditions. The findings unequivocally demonstrate that the augmentation of the protective properties of the rust layer is directly correlated with an increase in Mo content, transitioning from 0.5 to 1.5 wt.%. This transition is most evident in the

reduction of the corrosion rate for the 3Ni-Mo steel, dropping from an initial 1.74 mm a^{-1} to a robust 1.31 mm a^{-1} after 768 h of corrosion exposure. The heightened Mo content expedites the formation of a stable and durable rust layer, significantly enriching the proportion of α-FeOOH within this protective layer. The stabilized rust layer of 3Ni-Mo weathering steel exhibits a distinct three-layer structure, comprising an outer layer primarily of γ-FeOOH, an intermediate layer mainly composed of Fe_2O_3/Fe_3O_4, and an inner layer predominantly composed of α-FeOOH and β-FeOOH. Additionally, an alkaline interface enriched with $NiFe_2O_4$ and $CuFe_2O_4$ develops between the inner layer and the substrate. Firstly, Mo promotes the deposition of MoO_2, MoO_3, and molybdate on both the inner layer and alkaline steel-rust interface to repair corrosion pits and fill cracks. Secondly, Mo facilitates the generation of compounds such as $NiFe_2O_4$ and $CuFe_2O_4$, which heightens the electronegativity of the intermediate rust layer and the steel-rust interface, preventing Cl^--induced interface acidification and pitting corrosion. The higher Mo content expedites the formation of this alkaline interface and promotes inner layer densification. Most significantly, Mo creates additional nucleation sites for hydroxide oxides through oxide formation, leading to the formation of nano-sized α-FeOOH and β-FeOOH within the inner layer thereby enhancing the stability and compactness of the inner layer. These synergistic effects fortify the resilience of 3Ni-Mo advanced weathering steel in corrosive environments, ultimately strengthening its capacity to withstand environmental challenges.

Graphical abstract

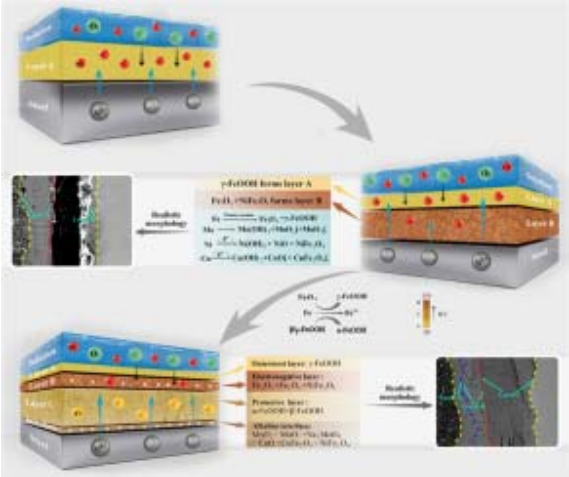

Download: Download high-res image (253KB)
Download: Download full-size image

Keywords

3Ni-Mo weathering steel; Corrosion behavior; Corrosion-resistant mechanisms; Stable rust layer

1. Introduction

Weathering steels, fortified with corrosion-resistant elements, provide a promising solution to meet the growing demand for steel materials in severe marine atmospheric corrosion environments with high Cl^- concentrations while maintaining mechanical properties [1], [2], [3], [4]. The meticulous composition design of weathering steels plays a crucial role in establishing a rust layer capable of withstanding intrusion by Cl^-, thus ensuring the viability of coating-free weathering steels [5], [6], [7], [8]. In the 1990s, Japanese researchers pioneered the development of 3Ni weathering steel, characterized by its composition of 3 %Ni + 0.4 % Cu [9]. This innovative formulation introduced new frontiers for utilizing weathering steel in marine atmospheric conditions. Exhaustive atmospheric exposure experiments spanning nine years demonstrated the exceeding twenty-fold enhancement of the 3Ni weathering steel in corrosion resistance in comparison to traditional weathering steel [10]. This significant advancement received worldwide recognition, establishing 3Ni steel as a premier candidate for deployment in marine atmospheric environments [11], [12], [13], [14].

While conventional 3Ni weathering steel is suitable for many applications, enhancing the corrosion resistance of 3Ni steel, particularly its performance in high-temperature, high-humidity, and high-salinity environments, remains crucial for the design and development of premium coating-free weathering steels. Studies indicate that the rust layer on the surface of Ni-advanced steel in harsh marine atmospheres is notably thicker and uneven. This allows corrosive Cl^- to permeate into the steel substrate through defects, leading to localized acidification and pitting corrosion beneath the inner rust layer. Consequently, there is significant potential to improve the corrosion resistance of 3Ni steel by adjusting the structure of the rust layer [13,14]. Key factors for enhancing corrosion resistance involve inhibiting the acidification of the interface between the rust layer and steel substrate (steel-rust interface) and preventing Cl^- into the outer rust layer [12]. When atmospheric corrosion takes place in humid conditions, the pH level decreases due to hydrolysis. In conventional weathering steels, the rust layer primarily composed of FeOOH carries a positive charge by bonding with H^+, thereby attracting anions that can permeate the substrate [15]. In contrast, the internal rust layer of 3Ni weathering steel encompasses negatively charged $Ni_xFe_{3-x}O_4$ phases, which actively repels Cl^- from the steel-rust interface and provides nucleation sites for the development of $Fe(O, OH)_6$ nanonetworks, leading to the creation of a compact film comprising fine particles [16], [17], [18], [19], [20]. This Cl-repelling rust layer presents an optimal configuration for weathering steel deployment in marine atmospheres, though it presents two distinct challenges. Firstly, during the initial corrosion stage, if Cl^- infiltrates the internal rust layer, causing the formation of β-FeOOH, it may lead to crack development within the rust layer [21,22]. Numerous references have pointed out the presence of substantial cracks in rust layers, serving as pathways for the diffusion of oxygen, various ions, and electrolytes [23], [24], [25]. Current research underscores the enhancement of stable α-FeOOH content. However, in marine atmospheric conditions, the emergence of β-FeOOH is inevitable. Consequently, mitigating the detrimental impacts caused by β-FeOOH emerges as a pivotal avenue to enhance corrosion resistance [26]. Secondly, if Cl^- enters the internal rust layer either during the initial corrosion stage or subsequent through cracks that act as conduits following the formation of the rust layer, the negatively charged rust layer containing $Ni_xFe_{3-x}O_4$ phases could impede the expulsion of

Cl^-. This will diminish the beneficial role of the rust layer in repelling Cl^- [12,19]. Currently, 3Ni steel finds successful application in coastal bridge infrastructure situated in moderately saline marine atmospheres, demonstrated by installations in Japan and Spain [27,28], satisfying the criteria for coating-free usage [12]. However, when subjected to more demanding environmental conditions like the Maldives, the corrosion rate of 3Ni steel during the first year of atmospheric exposure surged to 47.4 μm a^{-1}, exceeding the ideal standard of below 10 μm a^{-1} for coating-free weathering steel [16,17]. Consequently, the further optimization of 3Ni weathering steel remains imperative to ensure its uncompromised coating-free applicability in tropical marine settings.

Mo plays a pivotal role in enhancing the corrosion resistance of steel through multiple mechanisms [29], [30], [31], [32]. Primarily, during the corrosion process, the collaborative presence of MoO_4^{2-} and MoO_2, stemming from Mo, engenders an oxide film capable of repairing defects [30]. Additionally, when Mo is combined with Cu, the resultant formation of insoluble molybdate salts and Cu(I) compounds contributes to the development of a denser rust layer [33]. A comprehensive study conducted by Fan et al. [14] explored the influence of Mo content on the atmospheric corrosion of steel plates within a simulated high Cl^--tropical marine environment. As the Mo content increased from 0.34 to 1.23 wt.%, a noticeable augmentation in Mo^{6+} content within the inner layer of corrosion products was observed, accompanied by a decrease in Mo^{4+} content. Simultaneously, the presence of Cl^- within the rust layer exhibited a notable reduction. Elevated Mo content facilitated the enrichment of Ni elements and the formation of $NiFe_2O_4$ within the rust layer, synergistically driven by the effects of both Mo and Ni. This collaboration catalyzed the formation of protective corrosion products like α-FeOOH, Mo^{6+}, and $NiFe_2O_4$, contributing to the formation of a more condensed and stable rust layer. However, current research on the role of Mo in 3Ni steel remains limited, influenced by conventional microalloying principles [29,30]. The small quantities of added Mo are no longer adequate to meet the rigorous requirements for increased corrosion resistance in more severe marine atmospheric conditions. Consequently, the integration of elevated levels of Mo into 3Ni steel and the undertaking of comprehensive and systematic research assume paramount significance.

In this work, three types of Ni-advanced weathering steel with different Mo contents are designed, and their atmospheric corrosion mechanism was studied by microstructural characterization, electrochemical test, and cyclic corrosion test. The rust layer underwent thorough characterization of its phase structure and chemical compositions through advanced techniques such as scanning electron microscopy (SEM), X-ray diffraction (XRD), transmission electron microscopy (TEM), X-ray photoelectron spectroscopy (XPS), and Raman spectroscopy. The obtained results offer valuable insights and data support, contributing significantly to the design of innovative Ni-advanced steel that boasts enhanced protective properties against corrosion.

2. Experimental procedures

2.1. Materials

Utilizing the chemical composition design outlined in Table 1, three distinct variations of the 3Ni series Ni-advanced steel were meticulously prepared and denoted as 3Ni-0.5Mo steel, 3Ni-1Mo steel, and 3Ni-1.5Mo steel. The initial experimental steel was fabricated through vacuum induction melting and cast into ingots. The homogenization process was conducted at 1200 °C for 12 h. Then, the obtained ingots were subjected to forging, transforming them into billets with dimensions of 100 mm × 90 mm × 80 mm. Following another homogenization process at 1200 °C for 2 h, these billets were hot rolled to steel plates with a thickness of 12 mm. This rolling started at an initial temperature of 1150 °C and concluded at a final temperature of 890 °C. These rolled plates were subsequently air-cooled to room temperature.

Table 1. Chemical composition of 3Ni-Mo weathering steels (wt.%).

Steels	C	Si	Mn	P	S	Ni	Cu	Mo	Fe
3Ni-0.5Mo	0.10	0.28	1.04	0.007	0.003	3.01	0.27	0.51	Bal.
3Ni-1Mo	0.10	0.28	1.03	0.008	0.003	3.02	0.28	1.03	Bal.
3Ni-1.5Mo	0.093	0.28	1.03	0.008	0.003	3.04	0.27	1.52	Bal.

2.2. Determination of surface work function

To elucidate the influence of alloying elements on the corrosion resistance of the weathering steel matrix, first-principles calculations based on density functional theory (DFT) were employed to determine. Specifically, the surface electronic work function of the experimental steel was determined using this methodology. The calculations were conducted utilizing the Vienna *Ab-initio* Simulation Package (VASP) software, employing a comprehensive all-spin-polarized DFT framework [34]. These calculations adhered to the stringent Generalized Gradient Approximation (GGA) framework, employing the Perdew–Burke–Ernzerhof (PBE) functional [35,36]. The description of ionic cores utilized Projected Augmented Wave (PAW) potentials [37,38], while a plane-wave basis set with a kinetic energy cutoff of 500 eV was employed to account for valence electrons. The valence electron configurations employed in this study encompassed $4s^2 3d^6$ (Fe), $4s^2 3d^8$ (Ni), $4s^1 3d^5$ (Cr), and $5s^1 4d^5$ (Mo). The Gaussian smearing method was implemented, facilitating the partial occupation of Kohn-Sham orbitals within a range of 0.02 eV. The self-consistency of electronic energy was ensured when the energy change was less than 10^{-6} eV. This meticulous approach provided a comprehensive foundation for the subsequent analysis.

2.3. Cyclic corrosion tests

Cyclic corrosion tests (CCT) were meticulously conducted using a CK-901S composite salt spray chamber. To calculate the corrosion rate and analyze the corrosion product, samples with dimensions of 30 mm × 20 mm × 1 mm were employed. In addition,

samples with dimensions of 10 mm × 10 mm × 3 mm were utilized for corrosion product morphology characterizations and electrochemical measurements. Each test group consisted of three parallel samples to ensure the robustness of the experiment. The samples were to be stepwise polished using 200–800# SiC sandpapers, followed by being degreased in acetone, and then dehydrated in anhydrous ethanol post-rinsing with deionized water. Before the cyclic corrosion tests, the initial weight of each sample was carefully measured using an analytical balance with an accuracy of 10^{-4} g. Following this, a standardized 40 μL cm^{-2} droplet of a 3.5 wt.% NaCl solution was uniformly applied to the surface of each sample. Subsequently, the samples were placed within a controlled environment with a temperature of 40 °C and a relative humidity of 80 % [14]. The corrosion cycles were judiciously scheduled at specific intervals, specifically 96, 192, 384, and 768 h, thereby constituting a CCT cycle every 12 h.

The samples, subjected to varying corrosion cycles, underwent subsequent treatment. They were initially rinsed with deionized water and dried with anhydrous ethanol. A rust removal solution (500 mL deionized water + 500 mL 12 mol L^{-1} hydrochloric acid solution + 3.5 g hexamethylenetetramine) was then applied to effectively remove rust layers from the sample surfaces. Post-rust removal, the weight of samples was measured using an analytical balance to record weight loss. The samples were encapsulated with epoxy resin for observation. The cross-sectional surfaces were ground using SiC sandpapers (200#–2000#), followed by mechanical polishing and carbon coating.

2.4. Electrochemical tests

The prepared steels were wire cut into samples with dimensions of 10 mm × 10 mm × 3 mm. These samples underwent a gradual polishing process, followed by dehydration using anhydrous ethanol, and were then placed in a drying oven for 24 h. An insulated copper wire was connected to the back of samples using conducting resin to avoid undesirable ohmic effects. After that, all samples were embedded in epoxy resin, leaving an exposed surface area of 1 cm^2. Polarization curves (PD) and electrochemical impedance spectroscopy (EIS) tests were conducted using a typical three-electrode system [13], including a saturated calomel electrode (SCE) as the reference electrode, a platinum electrode as the counter electrode, and the working electrode (with an exposed area of 1 cm^2). Open-circuit potential tests were performed until the electrode reached a steady state (OCP variation rate ≤0.5 mV min^{-1}). The polarization curves were recorded with a scan rate of 0.167 mV s^{-1}. EIS measurements were performed at OCP in a frequency range of 10^{-2} to 10^5 Hz. The EIS data were fitted and analyzed using ZSimpWin 3.10 software. The electrolytes used for these tests matched the 3.5 wt.% NaCl solutions to simulate the marine environment. To be emphasized, all electrochemical tests were repeated three times to guarantee precision and consistency.

2.5. Microstructural characterization

Samples obtained through wire cutting, with dimensions of 10 mm × 10 mm × 3 mm, underwent a systematic preparation process. Initially, they underwent progressive polishing using sandpaper ranging from 200 to 2000 grit, followed by mechanical polishing. Subsequently, the samples were etched using a 4 vol.% nitric acid alcohol

solution for 8 s. Microstructural characterization was performed using the ZEISS ULTRA 55 field emission scanning electron microscope (SEM), accompanied by element distribution analysis through energy-dispersive spectroscopy (EDS). For electron backscatter diffraction (EBSD) characterization, samples with dimensions of 3 mm × 4 mm × 5 mm were extracted along the rolling direction. After grinding, electrochemical polishing was executed using a 10 vol.% perchloric acid ethanol solution for 25 s, with a voltage of 15 V and a current of 1 A. The polished surface underwent scanning (voltage 20 kV, step size 0.4 μm) via the EBSD probe integrated into the ZEISS ULTRA 55. The data post-processing was performed on the AztecCrystal software. For compositional analysis of the rust layer, micro-Raman spectroscopy was employed on rusted samples after microscopic observation. The output power ranged from 0.5 to 2.5 mW, with a spectral acquisition time of 30 s and a shift range spanning 0 to 1800 cm^{-1}. The peak positions of the rust layer were utilized as references for phase identification, as detailed in Table 2 [39,40].

Table 2. The phase in the rust layer corresponding to the peak in Raman spectroscopy.

Phase	**Peak position (cm^{-1})**
Lepidocrocite (γ-FeOOH)	217, 251, 655, 713, 1300
Goethite (α-FeOOH)	203, 244, 300, 387, 399, 415, 480, 552, 684, 1002, 1113, 1304
Akaganeite (β-FeOOH)	308, 389, 499, 539, 609, 1410
Magnetite (Fe_3O_4)	306, 538
Hematite (Fe_2O_3)	228, 250, 294, 502,1330
Maghemite (γ-Fe_2O_3)	Broadband between 339 and 386, 461 and 512, 671, and 717, 1430

Rust layers were derived from the corroded samples through scraping using a blade, followed by grinding. Phase analysis was carried out employing a DMAX-RB 12 kW rotating anode X-ray diffraction (XRD) instrument (Cu *K*α, voltage 40 kV, current 150 mA, 2θ range 10°–90°, step size 0.02°, and interval 0.6 s). The corrosion products after different corrosion durations were analyzed utilizing the X-ray photoelectron spectroscopy (XPS) spectra and high-resolution transmission electron microscope (HRTEM, FEI Talos F200X instrument). Vickers microhardness was applied with a load of 10 gf. To prepare the powder samples for TEM observation, manual grinding was initially applied, followed by placing a small amount within a glass test tube containing alcohol. Ultrasonic agitation was then applied for 20 min. Subsequently, 2–3 drops of the well-mixed powder-alcohol mixture were drawn into a glass capillary and then dispensed onto a microgrid (Φ 3 mm) for 15 min.

3. Results

3.1. Microstructure characterization

Fig. 1 depicts the microstructural morphologies of the three 3Ni series advanced weathering steels enriched with Mo. Since both Ni and Mo are transition group elements, their electron shells are not entirely occupied, which prompts the formation of strong bonds and electron sharing to reach the steady state. This electronic arrangement leads to reinforced interatomic bonding strength, thereby elevating the activation energy for atomic diffusion and reducing the diffusion coefficient. As a consequence, the transition from austenite to ferrite experiences a delay, promoting the formation of granular bainite (GB) [41]. The bainite microstructure in the three steels is quite similar, characterized by the presence of granular along with a minor proportion of lath bainite (LB). With the increase of Mo content, the number of martensite/austenite (M/A) islands increases while their sizes become finer. Furthermore, Inverse pole figure (IPF) maps provide additional visual evidence that the addition of Mo has no significant effect on the crystal orientation within the grains of the 3Ni series advanced weathering steel.

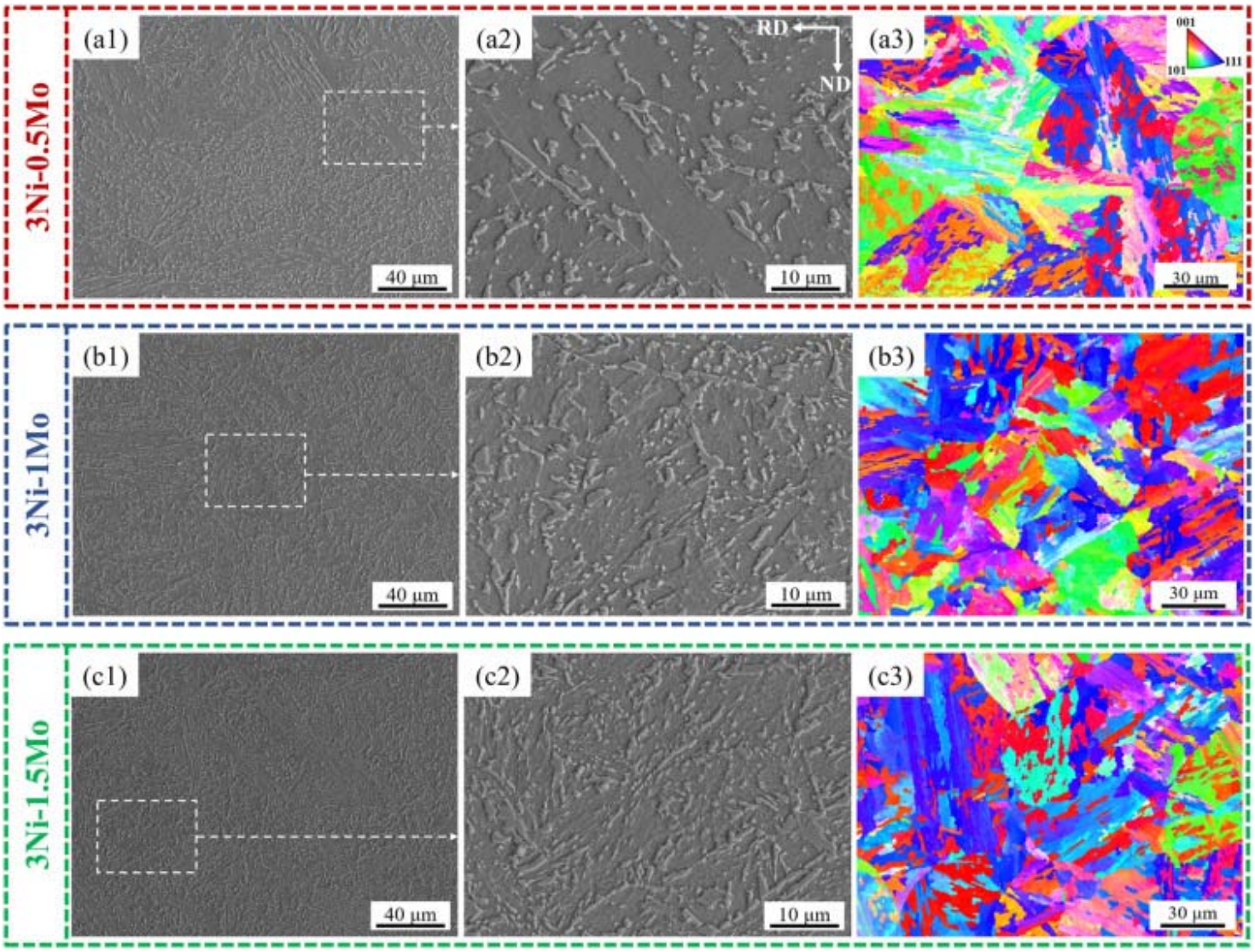

1. Download: Download high-res image (2MB)
2. Download: Download full-size image

Fig. 1. SEM micrographs and IPF maps of the prepared steels: (a) 3Ni-0.5Mo, (b) 3Ni-1Mo, and (c) 3Ni-1.5Mo.

3.2. Electrochemical properties of bare steels

Fig. 2(a) displays the polarization curves of the three experimental steels measured in a 3.5 wt.% NaCl solution. As indicated in Fig. 2(a), all curves exhibit consistent shapes, implying similar electrochemical mechanisms. The anodic region signifies the occurrence of activation dissolution, while the cathodic region is mainly associated with oxygen reduction and hydrogen evolution reactions [42]. Within the cathodic region, the polarization curves of the three experimental steels almost overlap, indicating the minimal impact of varying Mo content on the cathodic reaction of the 3Ni series advanced weathering steel. In addition, two basic electrochemical parameters, i.e., the corrosion

potential (E_{corr}) and corrosion current density (I_{corr}), are determined from PD curves based on the Tafel fitting (VersaStudio software), and the results are plotted in Fig. 2(b). Elevated Mo content induces a positive shift in the anodic polarization curves, effectively suppressing anodic activation dissolution. The positive shift combined with the decrease of corrosion current density indicates a reduction in thermodynamic and kinetic tendencies for corrosion [43]. Consequently, the corrosion resistance is enhanced.

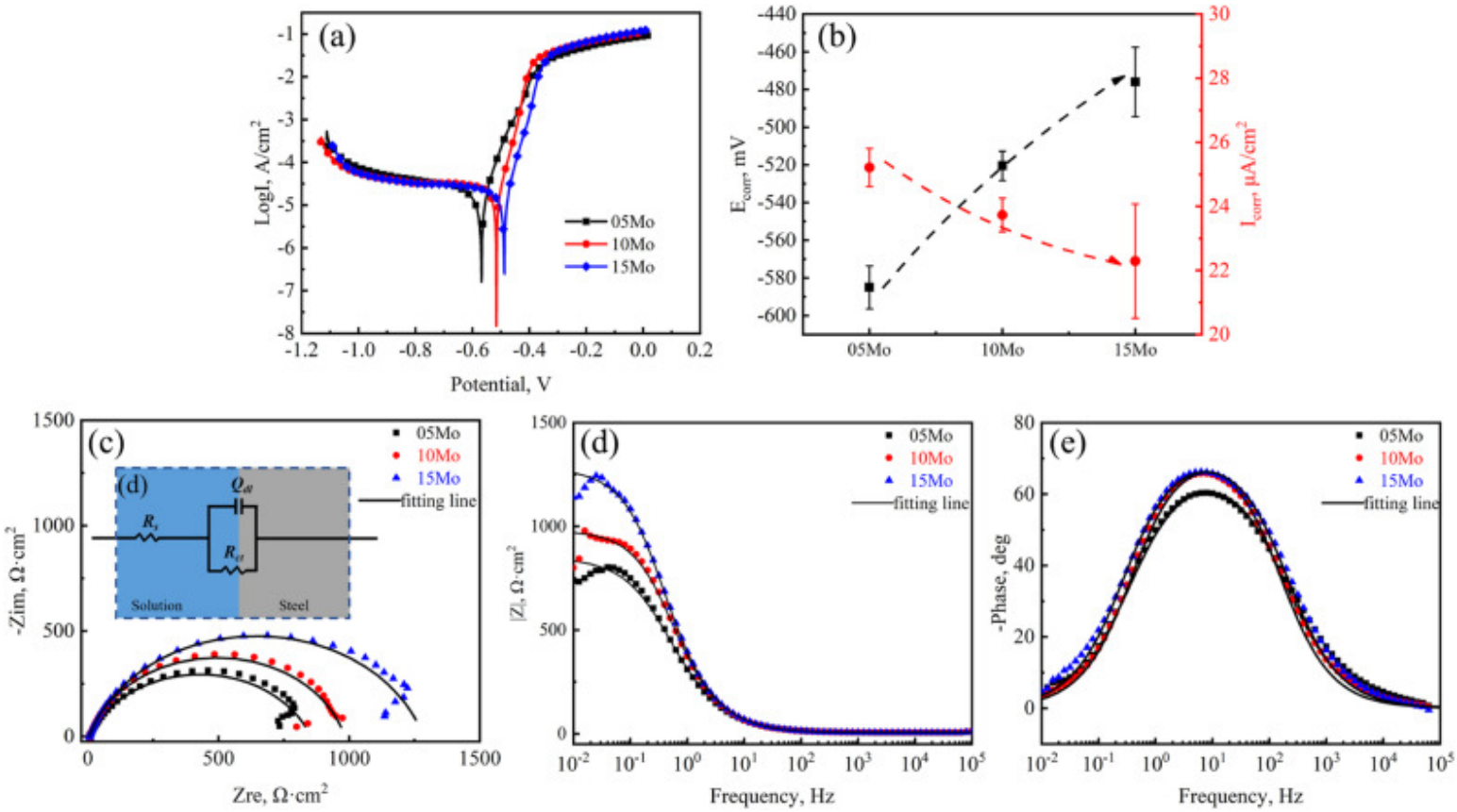

1. Download: Download high-res image (555KB)
2. Download: Download full-size image

Fig. 2. (a, b) The potentiodynamic polarization curves and (c–e) EIS curves of the prepared steels. The solid curves in (c–e) are the simulated results obtained by Zsimpwin software.

The EIS measurements were carried out to shed more light on the effects of Mo content on the corrosion resistance. Fig. 2(c–e) displays the EIS curves for the three experimental steels. It can be observed from Fig. 2(c) that all Nyquist plots exhibit a single capacitive loop, generally associated with one capacitive time constant. In addition, the diameter of the capacitive loop corresponds to the resistance; a larger diameter generally means a higher resistance [44]. As depicted in Fig. 2(c), the radius of the capacitive arc progressively increases with higher Mo content, demonstrating that an increase in the Mo content can improve corrosion resistance. Besides, the impedance value at the lowest frequency can be used as a basic index to semi-quantitatively evaluate the corrosion

resistance since this value is close to the polarization resistance, and a higher value generally corresponds to a higher corrosion resistance [45]. According to Fig. 2(d), the impedance value at 0.01 Hz increases with increasing the Mo content, indicating increased corrosion resistance. Furthermore, the Bode-Phase plot (Fig. 2(e)) displays one wide peak, indicating the presence of a one-time constant. Overall, Mo content plays a positive role in improving the corrosion resistance.

To quantitatively characterize the electrochemical behavior of the prepared steels, the equivalent circuit $R(QR)$ consisting of a one-time constant was employed to fit the measured impedance spectroscopy data. R_s is solution resistance, Q_{dl} is double-layer capacitance, and R_{ct} is charge transfer resistance. Due to the roughness of the sample surface, it is impossible to obtain the characteristic response of pure capacitance under ideal conditions. The surface of the working electrode exhibits a "dispersion effect". Therefore, the constant phase angle element Q is used as a substitute for the ideal capacitance C. The specific fitting values for each circuit parameter are summarized in Table 3. As shown in Table 3, the highest value of R_{ct} is observed for the 3Ni-1.5Mo steel, measuring at 1278 Ω cm², while the 3Ni-0.5Mo steel displays the smallest R_{ct} of just 846 Ω cm². These findings collectively underscore the improvement of corrosion resistance in 3Ni steels as the Mo content increases, which is consistent with the PD curves analysis.

Table 3. EIS fitting results of the prepared steels in 3.5 wt.%NaCl solution.

Steel	R_s (Ω cm²)	$Q_{dl} \times 10^{-4}$ (Ω^{-1} cm^{-2} s^n)	N	R_{ct} (Ω cm²)	χ^2 (10^{-3})
3Ni-0.5Mo	6.40	6.34	0.77	846	2.46
3Ni-1Mo	6.75	4.88	0.83	976	2.02
3Ni-1.5Mo	5.78	4.98	0.82	1278	1.90

3.3. Corrosion kinetics

Fig. 3 illustrates the corrosion weight gain, corrosion weight loss, and corrosion rate of the prepared steels after CCT. It can be observed from the corrosion weight gain curves (Fig. 3(a)), that the prepared steels exhibit roughly equal weight gain during the initial stages of corrosion (0–15 CCT cycles), with a gradually accelerating rate. After 15 CCT cycles, the corrosion weight gain rate begins to decrease, indicating that the formation of a rust layer on the surface alleviates the matrix corrosion. Besides, the corrosion weight gain rate of the 3Ni-1.5Mo steel is notably lower than that of the other two groups of steel, meaning that the 3Ni-1.5Mo steel exhibits the highest corrosion resistance. As corrosion progresses, the differences in corrosion weight gain become more pronounced, but the 3Ni-1.5Mo steel always maintains the lowest corrosion weight gain. In addition, Fig. 3(b) shows the corrosion weight loss rate as a function of time. To comprehensively analyze corrosion kinetics, the classical atmospheric corrosion power function model $V = A \times t^n$ was employed for fitting corrosion weight loss curves [46], [47], [48]. The parameter A represents the initial corrosion rate, and n indicates the protective quality of rust layers. In general, a lower n value implies a higher protection of the rust layer [49]. Table 4 summarizes the fitting results. The n of all steels is below 1, signifying the capacity of rust layers to impede further substrate corrosion. With higher Mo content

in 3Ni steels, both corrosion weight loss rate and n values decrease, indicating the improved protection of the rust layer. Fig. 3(c) illustrates the corrosion rates of the prepared steels at different corrosion periods. After 96 h of corrosion, the corrosion rate is lowest for 3Ni-0.5Mo steel at 2.09 mm y^{-1}, while 3Ni-1.5Mo steel exhibits the highest rate at 2.29 mm y^{-1}. However, as corrosion time extends, a reversal in corrosion rates occurs. After 192 h of corrosion, the corrosion rate of 3Ni-1.5Mo steel significantly decreases, indicating the rapid development of a protective rust layer. In contrast, the corrosion rate of 3Ni-0.5Mo steel continues to rise until a notable decrease after 384 h, suggesting a longer duration for its rust layer to exert protective effects. The corrosion rate of 3Ni-1Mo steel falls between the two, exhibiting a steady corrosion stage in the first 192 h, with a significant decrease after 384 h. Ultimately, after 768 h of corrosion, the corrosion rates further decrease to 1.74, 1.49, and 1.31 mm y^{-1} for 3Ni-0.5Mo, 3Ni-1Mo, and 3Ni-1.5Mo steels, respectively. Notably, the most significant reduction in corrosion rate is observed in 3Ni-1.5Mo steel, showcasing superior corrosion resistance.

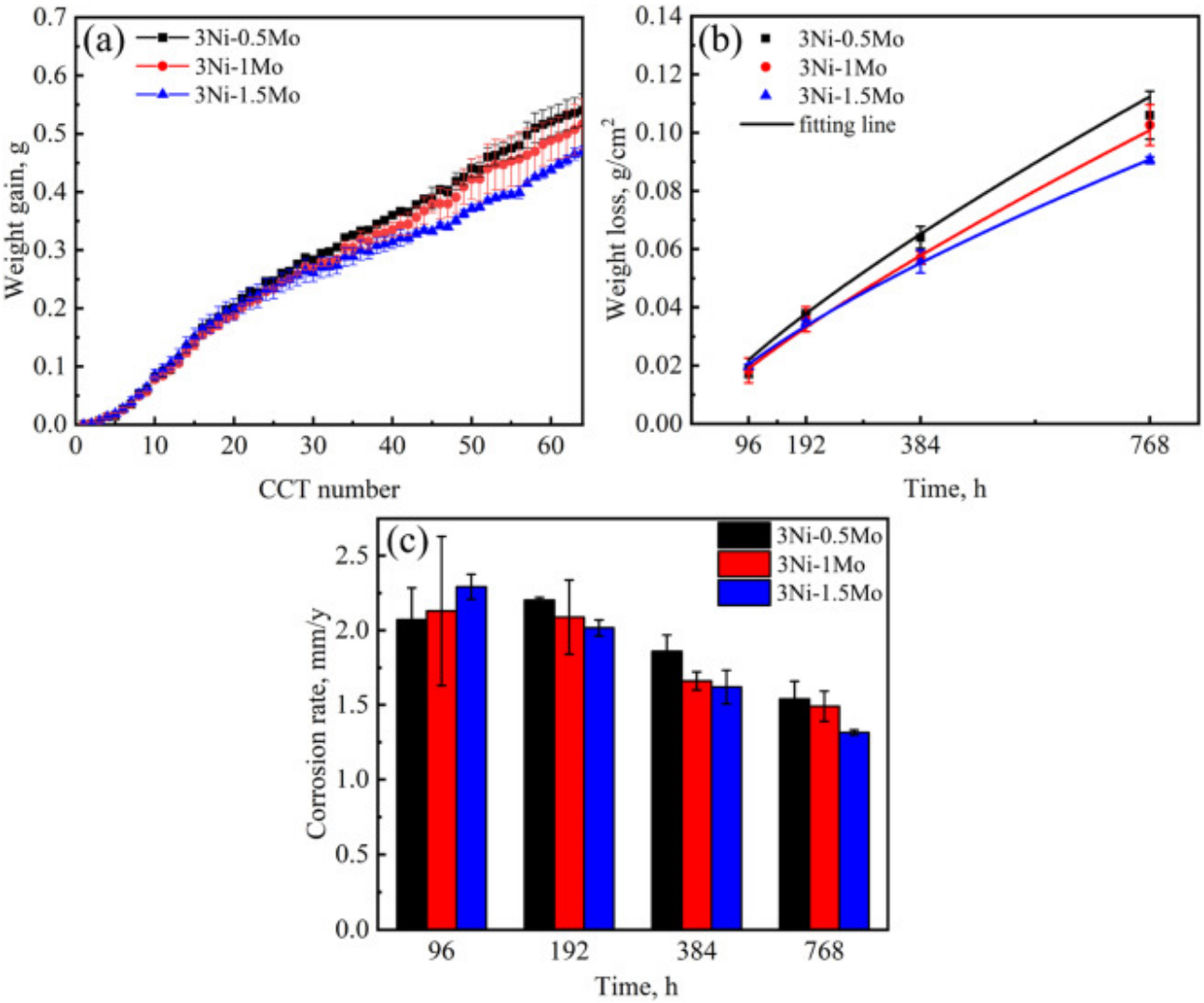

1. Download: Download high-res image (499KB)
2. Download: Download full-size image

Fig. 3. Corrosion kinetics curves of the prepared steels in 3.5 wt.% NaCl solutions: (a) weight gain, (b) weight loss, (c) corrosion rate.

Table 4. Fitting results of corrosion weight loss curves.

Steels	***A***	***n***	R^2
3Ni-0.5Mo	6.10×10^{-4}	0.78	0.96
3Ni-1Mo	1.66×10^{-4}	0.75	0.99
3Ni-1.5Mo	7.76×10^{-5}	0.71	0.99

3.4. Rust layer structure and evolution

3.4.1. Cross-sectional morphologies and element distribution

Fig. 4, Fig. 5, Fig. 6 depict the cross-sectional microstructures and elemental distribution of experimental steels with varying Mo content after different corrosion periods. The analysis of the cross-sectional rust layer provides valuable insights into corrosion product evolution and patterns. In the initial corrosion stage (96 h), a notable gap exists between the rust layer and the matrix across all steels. This gap highlights weak bonding between the rust layer and the matrix during the initial corrosion stages, contributing to suboptimal corrosion resistance. During this period, the rust layer of the 3Ni-0.5Mo steel exhibits a bilayer structure, a common characteristic of weathering steels. The inner rust layer hosts many microcracks linking the steel matrix to the outer rust layer. These microcracks serve as pathways for the infiltration of O_2 and corrosive ions such as Cl^-, exacerbating matrix corrosion. As corrosion progresses to a relatively stable phase (384 h for 3Ni-0.5Mo steel and 192 h for 3Ni-1Mo and 3Ni-1.5Mo steels), a distinct three-layer structured rust layer emerges. From the outermost to the innermost aspect, these layers are labeled Layer A, Layer B, and Layer C, indicated by red arrows in Figs. 4(c), 5(b), and 6(b). Each layer exhibits distinctive morphological traits and thickness trends. Layer A, positioned as the rust layer's outermost stratum, showcases a loose configuration with voids and cracks. Layer B, while containing similar flaws, boasts a relatively smoother surface and more pronounced densification. Additionally, with extended corrosion time, the proportion of Layer B gradually diminishes. Emerging as the dominant component of the rust layer in a steady state, Layer C comprises a few penetrating microcracks, with its thickness increasing significantly as corrosion progresses. Distinguished by a darker hue compared to Layer B, Layer C distinctly demarcates from Layer B through a clear boundary line.

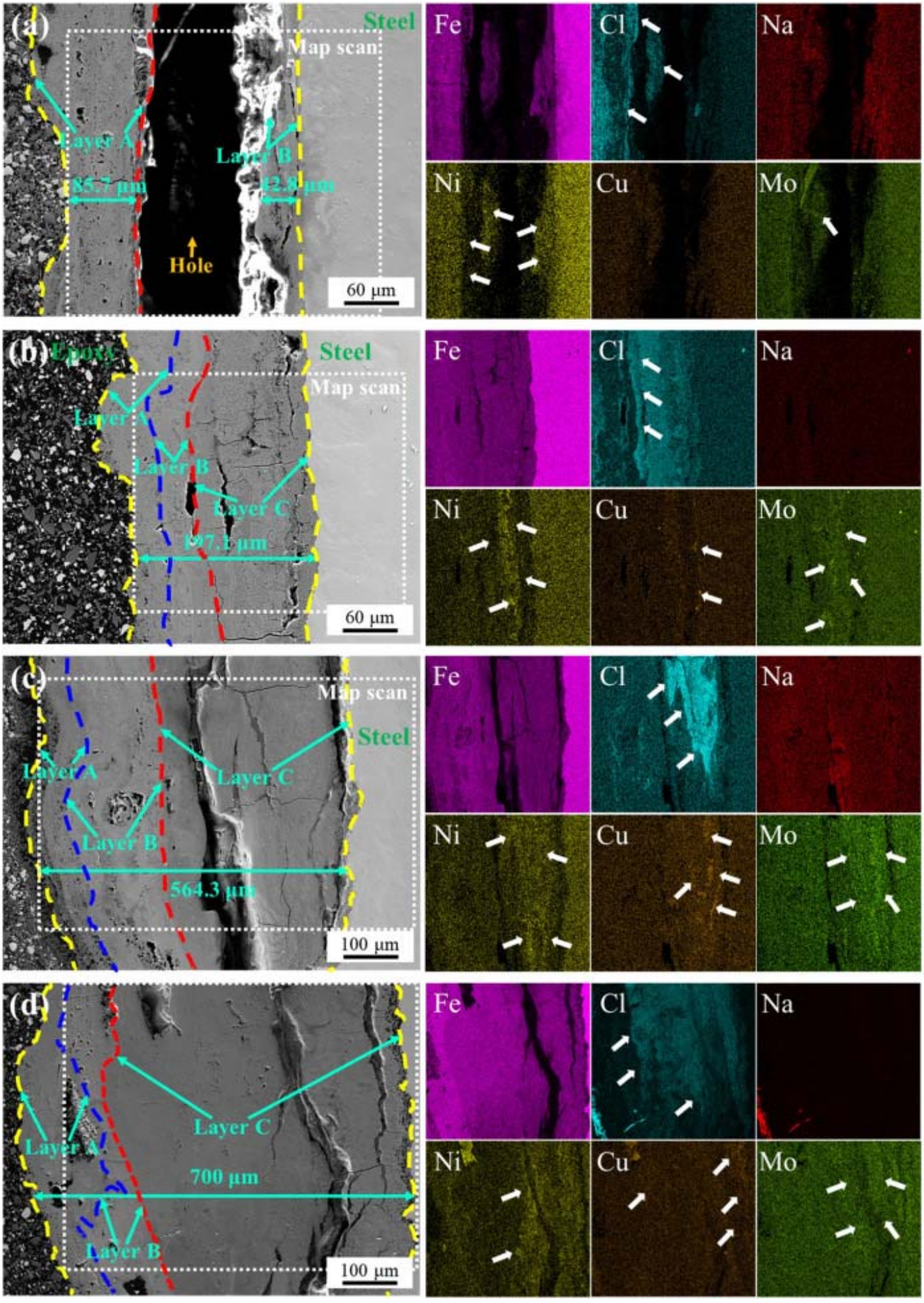
(a)
Steel
Map scan
Layer A
Layer B
85.7 µm
42.8 µm
Hole
60 µm
Fe
Cl
Na
Ni
Cu
Mo
(b)
Epoxy
Steel
Map scan
Layer A
Layer B
Layer C
197.1 µm
60 µm
Fe
Cl
Na
Ni
Cu
Mo
(c)
Map scan
Steel
Layer A
Layer C
Layer B
564.3 µm
100 µm
Fe
Cl
Na
Ni
Cu
Mo
(d)
Layer C
Layer A
700 µm
Layer B
100 µm
Fe
Cl
Na
Ni
Cu
Mo

1. Download: Download high-res image (4MB)
2. Download: Download full-size image

Fig. 4. Cross-sectional morphologies and elemental distribution of 3Ni-0.5Mo steel after different corrosion durations: (a) 96 h, (b) 192 h, (c) 384 h, and (d) 768 h.

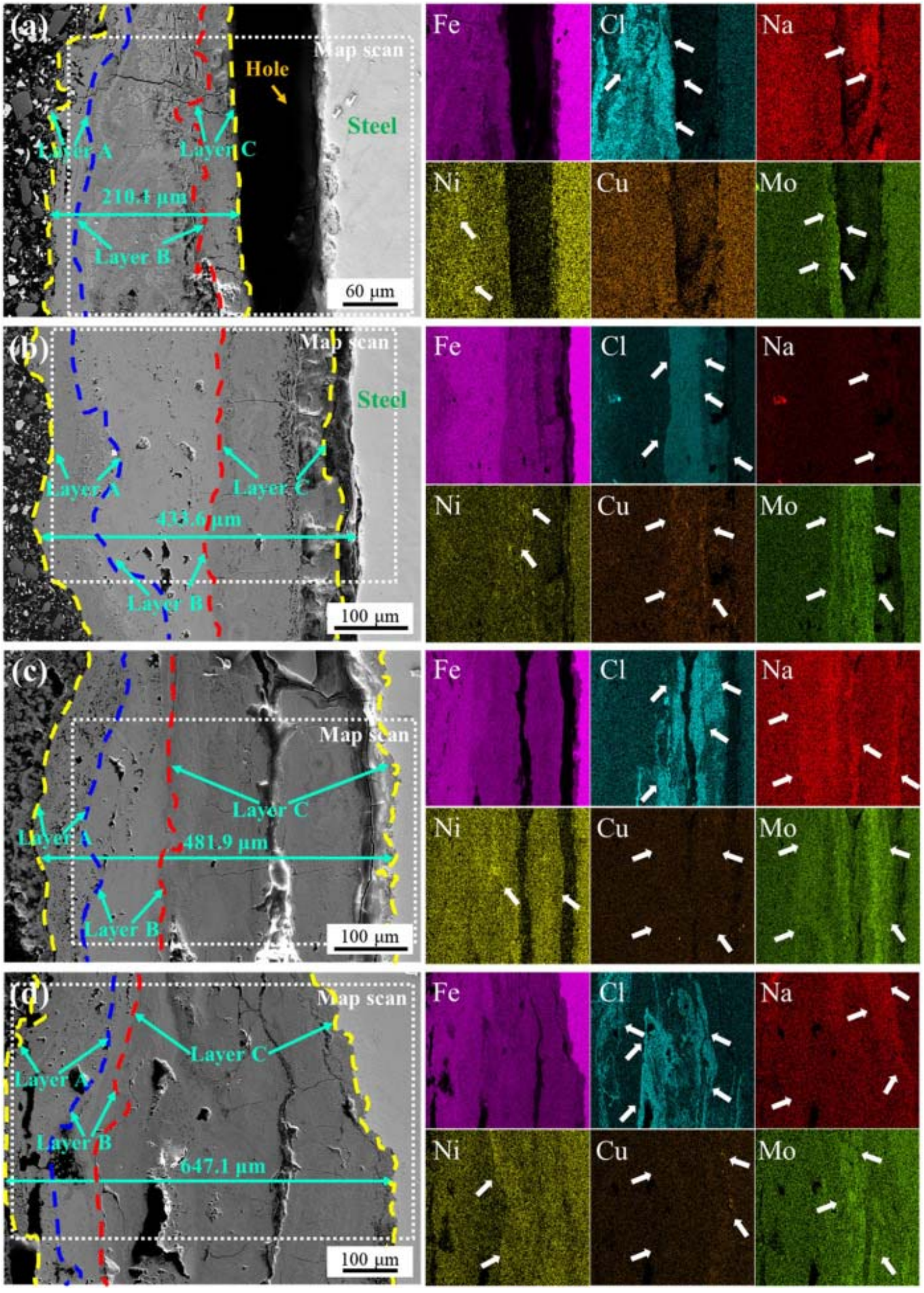
(a)
Map scan
Hole
Steel
Layer A
Layer C
210.1 μm
Layer B
60 μm
Fe
Cl
Na
Ni
Cu
Mo
(b)
Map scan
Steel
Layer A
Layer C
433.6 μm
Layer B
100 μm
Fe
Cl
Na
Ni
Cu
Mo
(c)
Map scan
Layer C
Layer A
481.9 μm
Layer B
100 μm
Fe
Cl
Na
Ni
Cu
Mo
(d)
Map scan
Layer C
Layer A
Layer B
647.1 μm
100 μm
Fe
Cl
Na
Ni
Cu
Mo

1. Download: Download high-res image (4MB)
2. Download: Download full-size image

Fig. 5. Cross-sectional morphologies and elemental distribution of 3Ni-1Mo steel after different corrosion durations: (a) 96 h, (b) 192 h, (c) 384 h, and (d) 768 h.

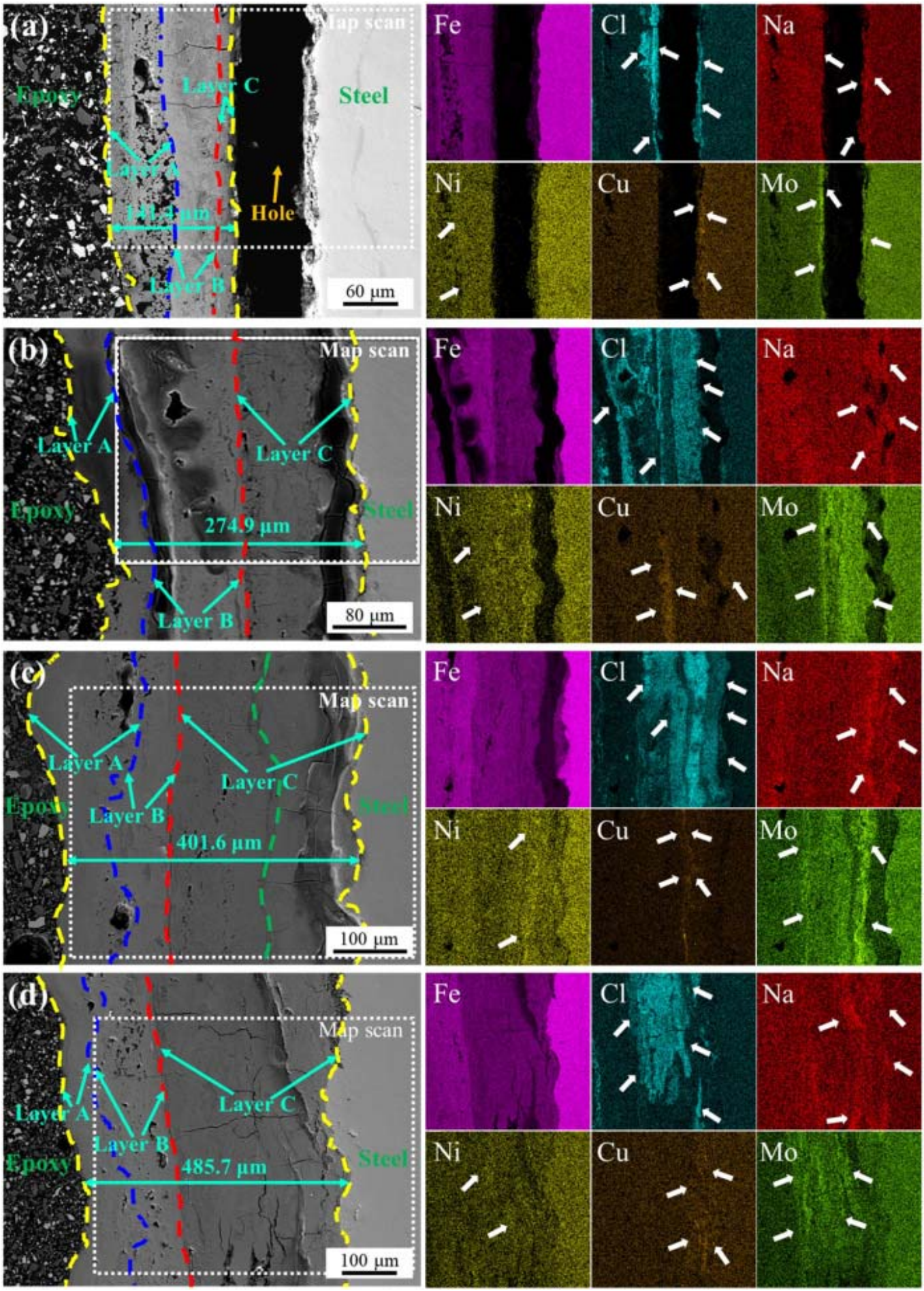
(a)
Map scan
Epoxy
Layer C
Steel
Layer A
141.4 µm
Hole
Layer B
60 µm
Fe
Cl
Na
Ni
Cu
Mo
(b)
Map scan
Layer A
Layer C
Epoxy
Steel
274.9 µm
Layer B
80 µm
Fe
Cl
Na
Ni
Cu
Mo
(c)
Map scan
Layer A
Layer C
Epoxy
Layer B
Steel
401.6 µm
100 µm
Fe
Cl
Na
Ni
Cu
Mo
(d)
Map scan
Layer A
Layer C
Layer B
Epoxy
485.7 µm
Steel
100 µm
Fe
Cl
Na
Ni
Cu
Mo

1. Download: Download high-res image (4MB)
2. Download: Download full-size image

Fig. 6. Cross-sectional morphologies and elemental distribution of 3Ni-1.5Mo steel after different corrosion durations: (a) 96 h, (b) 192 h, (c) 384 h, and (d) 768 h.

Irrespective of the stratified structure, the total rust layer thickness in all steel samples gradually increases with extended corrosion cycles. Taking the 3Ni-0.5Mo steel as an example, the total rust layer thickness expands from 182.5 μm at 96 h to 700 μm at 768 h. Similarly, for the 3Ni-1.5Mo steel, the total rust layer thickness grows from 141.4 μm at 96 h to 485.7 μm at 768 h. Interestingly, the rust layer thickness at 768 h demonstrates a decrease with higher Mo content (700 μm → 647.1 μm → 485.7 μm). Correlating this with corrosion rate results suggests that rust layers become more protective with increased Mo content.

Beyond the noticeable morphology stratification, the rust layer exhibits distinctive elemental distribution patterns. Elements including Ni, Mo, Cu, Na, and Cl display tendencies for enrichment within the rust layer, marked by white arrows in Fig. 4, Fig. 5, Fig. 6. Ni tends to distribute uniformly across the rust layer, while Mo is concentrated in Layer C. The distribution of Cu is not uniform, and it is concentrated at the steel-rust interface. The distribution of Na and Cl varies among different layers. During the stable rust layer stages of 3Ni-1Mo and 3Ni-1.5Mo steels (after 192 h), Na tends to concentrate in Layer B, Layer C near the substrate, and the steel-rust interface; Cl is enriched in Layer A and Layer C, while a depleted Cl region emerges in Layer B and the steel-rust interface.

3.4.2. Phase analysis of corrosion film products

To determine the phase composition of the rust layers in the three experimental steels, XRD was employed for phase analysis and semi-quantitative calculations of the rust layers at different corrosion time intervals [50], [51], [52], [53]. The rust layers in all three steels exhibit consistent phase compositions, including α-FeOOH, β-FeOOH, γ-FeOOH, and Fe_2O_3/Fe_3O_4, as shown in Fig. 7. The presence of NaCl arises from its accumulation within the rust layer pores during experimentation. As corrosion cycles increase, the α-FeOOH content gradually rises. This increase in thermodynamic stability and content of protective α-FeOOH effectively bolsters the corrosion resistance of the rust layer (Fig. 7(b, d, f)). Semi-quantitative calculations confirm that higher Mo content augments α-FeOOH content within rust layers. β-FeOOH forms in the acidic rust layer conditions with Cl^-. β-FeOOH exhibits high oxidizability and can readily undergo reduction during wet-dry cycles, generating amorphous intermediates that accelerate corrosion [54]. The γ-FeOOH phase demonstrates a gradual increase, representing an initial thermodynamically metastable product with strong reactivity. During the corrosion process, γ-FeOOH can act as a cathode in electrochemical reactions, leading to the formation of α-FeOOH or, in oxygen-depleted environments, the generation of Fe_3O_4 [50]. Due to the similar crystal structures of Fe_2O_3 and Fe_3O_4, XRD is unable to precisely distinguish between them. Hence, both are discussed. The contents of Fe_2O_3 and Fe_3O_4 gradually decrease with increasing corrosion cycles. Fe_3O_4 is also a thermodynamically metastable phase, but it is more stable than γ-FeOOH and has a

relatively compact structure. Meanwhile, Fe_3O_4 exhibits strong conductivity and is easily reducible. It can be mutually converted with γ-FeOOH or further oxidized into Fe_2O_3 [51].

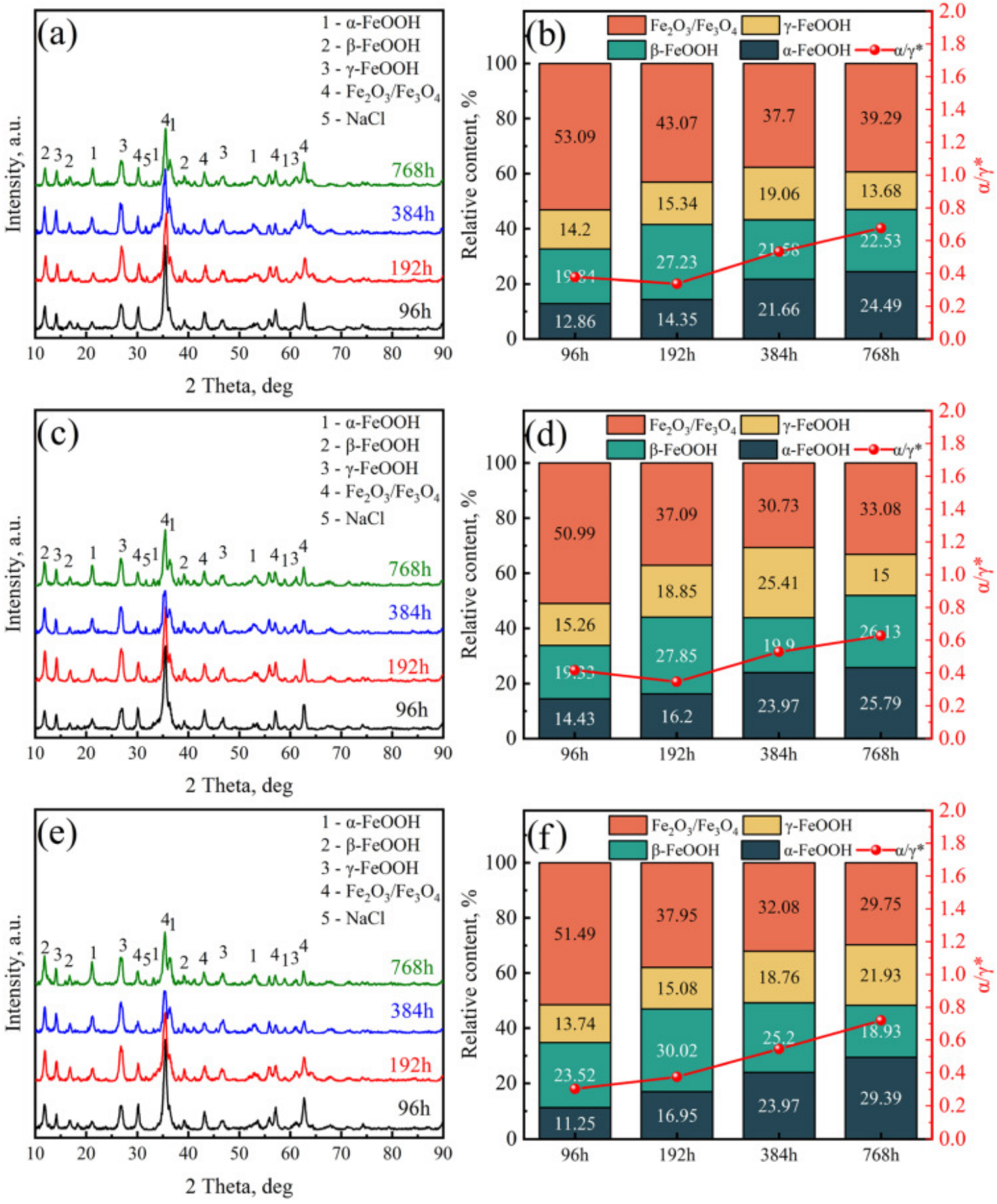
(a)
1 - α-FeOOH
2 - β-FeOOH
3 - γ-FeOOH
4 - Fe2O3/Fe3O4
5 - NaCl
768h
384h
192h
96h
Intensity, a.u.
2 Theta, deg
(b)
Fe2O3/Fe3O4
γ-FeOOH
β-FeOOH
α-FeOOH
α/γ*
Relative content, %
53.09
14.2
19.84
12.86
43.07
15.34
27.23
14.35
37.7
19.06
21.58
21.66
39.29
13.68
22.53
24.49
96h
192h
384h
768h
(c)
(d)
50.99
15.26
19.33
14.43
37.09
18.85
27.85
16.2
30.73
25.41
19.9
23.97
33.08
15
26.13
25.79
(e)
(f)
51.49
13.74
23.52
11.25
37.95
15.08
30.02
16.95
32.08
18.76
25.2
23.97
29.75
21.93
18.93
29.39

1. Download: Download high-res image (2MB)
2. Download: Download full-size image

Fig. 7. XRD patterns and semi-quantitative analysis of corrosion products for different corrosion durations of the prepared steels: (a, b) 3Ni-0.5Mo, (c, d) 3Ni-1Mo, and (e, f) 3Ni-1.5Mo.

In this study, the α/γ* ratio was utilized as a metric to assess the protective quality of the rust layers. Here, α signifies the proportion of α-FeOOH, while γ* represents the combined proportions of β-FeOOH and γ-FeOOH [24]. As the corrosion duration extends, the α/γ* ratio progressively rises. Among the steel groups, the 3Ni-1.5Mo steel demonstrates the highest α/γ* value. It is essential to emphasize that while the α/γ* value signifies the protective ability of the rust layer, it is not the sole determinant of corrosion resistance. The protective nature of the rust layer is also influenced by its physical structure.

Incorporating an analysis of rust layer cross-sections provides a more profound comprehension of rust formation and phase transformation processes. The fluctuations in phase content within the rust layer correspond remarkably to changes in its structural configuration. In the initial corrosion phases, a substantial portion of Fe dissolves, giving rise to Fe^{2+} that subsequently oxidizes into Fe^{3+}. This process leads to the formation of initial corrosion products, namely γ-FeOOH and Fe_3O_4, which constitute Layer A and Layer B. At the early stage of corrosion, at 96 h, the combined proportion of these two phases reaches over 60 %. As corrosion progresses, a significant number of α-FeOOH forms through the following Eqs. (1) and (2) [40].

$$\gamma - \mathrm{FeOOH} + \mathrm{H_2O} \leftrightarrow \mathrm{Fe(OH)_2} + \mathrm{H^+} + \frac{1}{2}\mathrm{O_2} + \mathrm{e^-} \quad (1)$$

$$\gamma\text{-FeOOH} \rightarrow \mathrm{FeO}_X\mathrm{(OH)}_{3-2X} \rightarrow \alpha\text{-FeOOH} \quad (2)$$

Simultaneously, influenced by both high Cl^- ion concentrations and the ensuing acidic environment, a substantial quantity of β-FeOOH forms via the sequence: $FeCl_2$ → β-$Fe_2(OH)_3Cl$ → GR1(Cl^-) → β-FeOOH [54]. This phase transformation leads to the establishment of a stable rust layer characterized by the composite structure of Layer A, Layer B, and Layer C. During this stage, the thickness of Layer C undergoes significant expansion, ultimately becoming the predominant constituent of the rust layer. As a result, the XRD results at 192 h demonstrate an increase in the relative content of α-FeOOH and β-FeOOH.

To further investigate the chemical states of the primary elements Fe, Ni, and Mo within the rust layer, XPS analysis was conducted on rust layers gathered at various corrosion stages, as depicted in Fig. 8. Evident is the consistency in major compounds across rust layers formed on all prepared steels during different corrosion periods. Fe predominantly appears in the forms of Fe_2O_3, Fe_3O_4, and FeOOH. For Ni, three chemical states manifest: $Ni(OH)_2$, NiO, and $NiFe_2O_4$. However, there is no distinct pattern observed in the major compounds of Ni. Mo consistently emerges as Mo^{4+} and Mo^{6+} species. As the rust layer

structure achieves greater stability in the corrosion deceleration phase, the relative content of Fe_3O_4 gradually diminishes, while Fe_2O_3 and FeOOH proportions elevate. The heightened Mo content within the matrix spurs Mo^{4+} to Mo^{6+} transformation, leading to a gradual increase in Mo^{6+} presence within the rust layer. Mo^{6+} in the form of $MoO4^{2-}$ serves as an anodic inhibitor, effectively reducing Cl^- ion adsorption sites and hindering anodic dissolution [55]. Drawing from the analysis conducted earlier, it is established that Cu elements precipitate at the steel-rust interface. As a result, no corrosion products of Cu were detected in the XPS analysis of the rust layer.

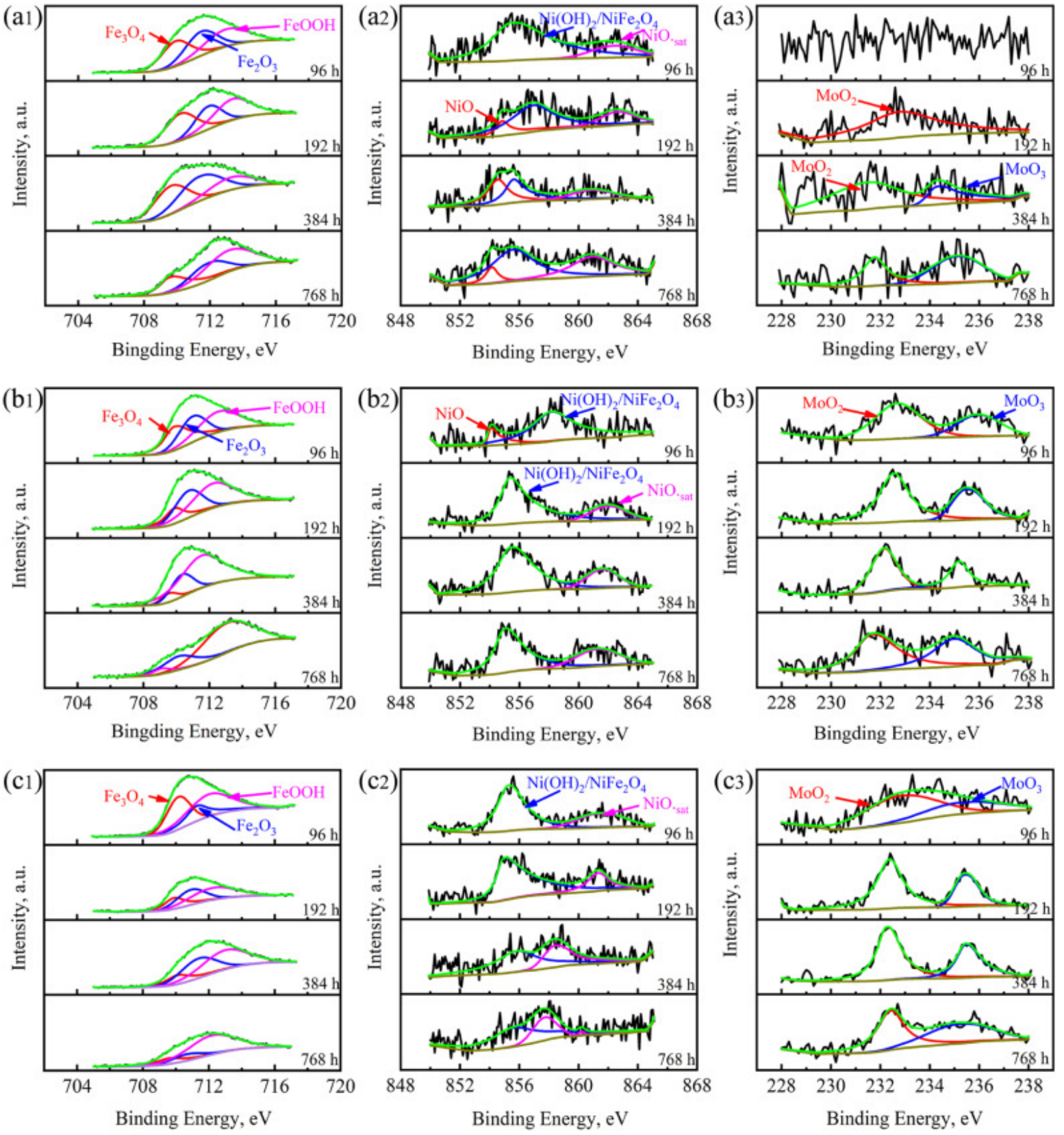
(a1)
Fe3O4
FeOOH
Fe2O3
96 h
192 h
384 h
768 h
Intensity, a.u.
704 708 712 716 720
Bingding Energy, eV
(a2)
Ni(OH)2/NiFe2O4
NiO-sat
NiO
96 h
192 h
384 h
768 h
Intensity, a.u.
848 852 856 860 864 868
Binding Energy, eV
(a3)
MoO2
MoO3
96 h
192 h
384 h
768 h
Intensity, a.u.
228 230 232 234 236 238
Bingding Energy, eV
(b1)
Fe3O4
FeOOH
Fe2O3
96 h
192 h
384 h
768 h
Intensity, a.u.
704 708 712 716 720
Bingding Energy, eV
(b2)
NiO
Ni(OH)2/NiFe2O4
NiO-sat
96 h
192 h
384 h
768 h
Intensity, a.u.
848 852 856 860 864 868
Binding Energy, eV
(b3)
MoO2
MoO3
96 h
192 h
384 h
768 h
Intensity, a.u.
228 230 232 234 236 238
Bingding Energy, eV
(c1)
Fe3O4
FeOOH
Fe2O3
96 h
192 h
384 h
768 h
Intensity, a.u.
704 708 712 716 720
Binding Energy, eV
(c2)
Ni(OH)2/NiFe2O4
NiO-sat
96 h
192 h
384 h
768 h
Intensity, a.u.
848 852 856 860 864 868
Binding Energy, eV
(c3)
MoO2
MoO3
96 h
192 h
384 h
768 h
Intensity, a.u.
228 230 232 234 236 238
Binding Energy, eV

1. Download: Download high-res image (2MB)
2. Download: Download full-size image

Fig. 8. XPS spectra of Fe $2p_{3/2}$, Ni $2p_{3/2}$, and Mo $3d_{3/2}$ of the prepared steels after different corrosion durations: (a) 3Ni-0.5Mo, (b) 3Ni-1Mo, and (c) 3Ni-1.5Mo.

4. Discussion

4.1. The relationship between the three-layer structure and element distribution of the rust layer

Low-alloy weathering steel primarily relies on the development of rust layers during the corrosion process to combat atmospheric corrosion, thereby partially isolating electrolytes and corrosive ions [1]. In contrast to the dual-layer structure observed in conventional weathering steel, the cross-sectional morphology of rust layers (as shown in Fig. 4, Fig. 5, Fig. 6) verifies the distinctive presence of a three-layer configuration within the stable rust layers of the three examined weathering steels. Furthermore, the elemental distribution within these rust layers follows specific patterns as deduced from the surface scan findings. In addition to Fe, alloying elements such as Ni and Mo also engage in the formation of phases with different physicochemical properties in the rust layer through electrochemical reactions with the help of corrosive mediums. These phases include oxides, hydroxides, and hydroperoxides, which collectively impact the corrosion resistance of different sections or the entirety of the rust layer. This phenomenon is corroborated by the quantitative elemental characterization of typical positions within the rust layer, namely Layer A, Layer B, and Layer C (as illustrated in Fig. 9(a)). The trends in the distribution of primary elements are depicted in Fig. 9(b–d), highlighting perceptible variations in element distribution in each layer of the rust layer. The quantitative results are shown in Tables S1–S3. The contents of Ni and Cu gradually increase from Layer A to Layer C, with Ni showing a more gradual increase. Meanwhile, Cu tends to accumulate more near the steel-rust interface closer to the substrate (Point C-S), which aligns with the above surface scan results (Fig. 4, Fig. 5, Fig. 6). The Mo content within Layer C significantly surpasses that present in Layer A and Layer B. Furthermore, the Mo content in Layer C escalates in tandem with the augmentation of Mo content in the experimental steel. In Layer A, the Cl content does not exhibit a discernible pattern, while in Layer B, it consistently maintains a relatively low level, generally below 0.5 wt.%. It is noteworthy that at Point C within Layer C, the Cl content significantly rises, surpassing 6 wt.% in some positions. However, this content precipitously drops at Point C-S near the substrate. Additionally, the Cl content at Point C-S experiences further reduction with heightened Mo content in the steel. As an illustration, following 768 h of corrosion, the Cl content at Point C-S for the 3Ni-0.5Mo steel measures to be 1.13 wt.%, whereas for the 3Ni-1.5Mo steel, it dwindles to a mere 0.12 wt.%. Intriguingly, as Mo content increases, the Na content at Point C-S demonstrates an inverse trajectory in comparison to Cl. For instance, post 768 h of corrosion, the Na content at Point C-S for the 3Ni-0.5Mo steel reaches 0.51 wt.%, while for the 3Ni-1.5Mo steel, it increases to 1.2 wt.%, approximately tenfold that of Cl at the same location. These observations robustly imply the formation of an alkaline steel-rust interface. By amalgamating the insights derived from the evolution of rust layer structure in Section 3.4.1, it becomes evident that when the matrix contains 1 wt.% or 1.5 wt.% Mo, a rust layer with a stable structure and an alkaline steel-rust interface enriched with Na can be formed after 192 h. Importantly, as the Mo content in the matrix increases, the enhancing effects of the alkaline interface become more pronounced. This heightened alkaline interface effectively mitigates the corrosion acceleration resulting from localized acidification,

thereby alleviating the occurrences of pitting and localized corrosion (Figs. S1 and S2 in Supporting Information) [56].

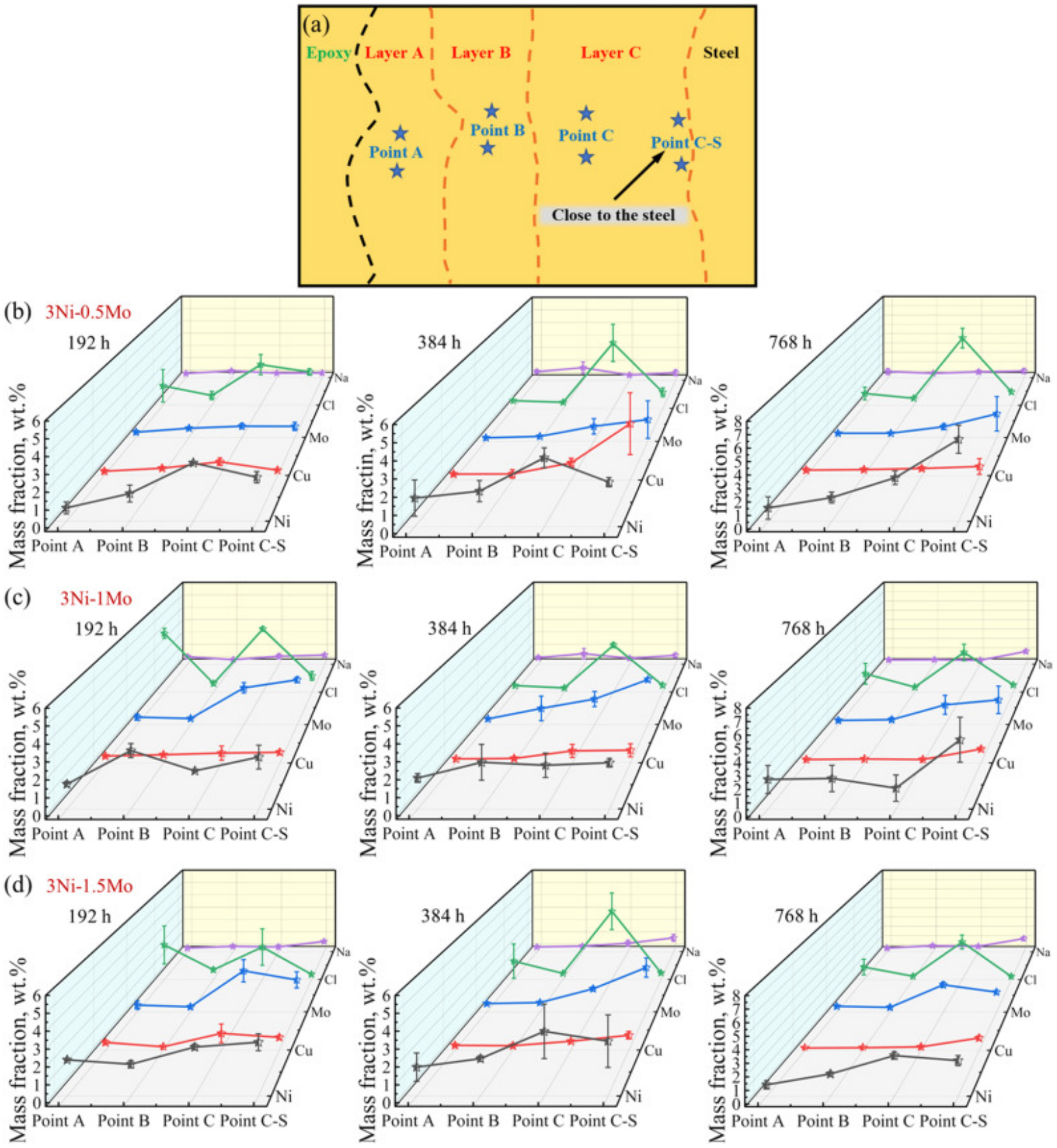
(a)
Epoxy
Layer A
Layer B
Layer C
Steel
Point A
Point B
Point C
Point C-S
Close to the steel
(b) 3Ni-0.5Mo
192 h
384 h
768 h
(c) 3Ni-1Mo
192 h
384 h
768 h
(d) 3Ni-1.5Mo
192 h
384 h
768 h
Mass fraction, wt.%
Mass fractin, wt.%
Point A
Point B
Point C
Point C-S
Na
Cl
Mo
Cu
Ni

1. Download: Download high-res image (1MB)
2. Download: Download full-size image

Fig. 9. (a) Schematic diagram of EDS points in the rust layer and distribution of main elements at different locations: (b) 3Ni-0.5Mo, (c) 3Ni-1Mo, and (d) 3Ni-1.5Mo.

4.2. The effect of Mo element on the compactness of the rust layer

The cross-sectional morphology of the rust layer in Section 3.4.1 shows that increasing the Mo content is favorable for the rust layer to reach a stable state of a three-layer structure in a shorter period. The electrochemical properties of the rust layer also prove this (Fig. S3). The elemental distribution patterns outlined in Section 4.1 provide initial indications of distinct potential chemical reactions unfolding across different layers of the rust layer. Thus, for a comprehensive elucidation of the anticorrosion mechanism of this three-layer configuration, a deeper examination of physical attributes and phase distribution for each layer becomes imperative. In this regard, microhardness assessments of each layer were conducted via a microhardness tester, as depicted in Fig. 10, Fig. 11, Fig. 12. Furthermore, meticulous analyses of the phase composition at corresponding positions were conducted utilizing micro-Raman and EDS techniques, as illustrated in Fig. 11, Fig. 12, Fig. 13. It is important to acknowledge that the microhardness tester was applied with a load of 10 gf. Despite the potential for some measurement error, the microhardness values can still effectively reflect the relative compactness of the rust layers. The external Layer A, characterized by its porous structure, exhibits a range of approximately 15–40 HV in microhardness. This layer primarily comprises γ-FeOOH (density of 4.1 g cm^{-3}). The intermediate Layer B, as the most compact layer, exhibits microhardness values 3–5 times higher than Layer A, ranging from 80 to 120 HV. This layer is primarily composed of Fe_2O_3/Fe_3O_4 (density of 4.88/5.2 g cm^{-3}). The inner Layer C, positioned closer to the substrate, records a microhardness in the range of 25–40 HV. Notably, this value escalates with increased Mo content. This layer is predominantly constituted by α-FeOOH (density of 4.3 g cm^{-3}) and β-FeOOH (density of 3.0 g cm^{-3}).

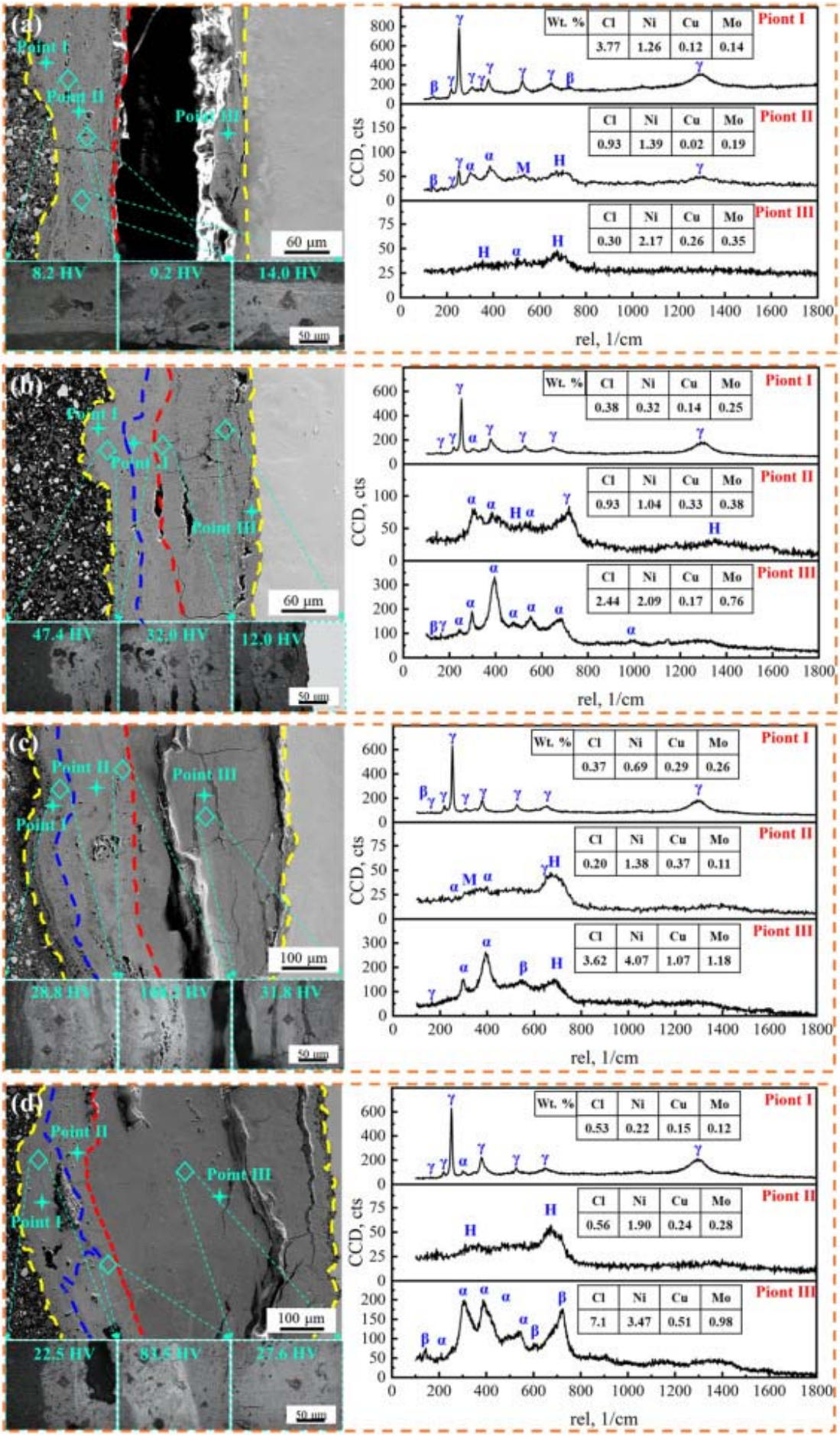
(a)
Point I
Point II
Point III
60 μm
8.2 HV
9.2 HV
14.0 HV
50 μm
Wt. %
Cl
Ni
Cu
Mo
Piont I
3.77
1.26
0.12
0.14
Piont II
0.93
1.39
0.02
0.19
Piont III
0.30
2.17
0.26
0.35
CCD, cts
rel, 1/cm
(b)
Point I
Point II
Point III
60 μm
47.4 HV
32.0 HV
12.0 HV
50 μm
Piont I
0.38
0.32
0.14
0.25
Piont II
0.93
1.04
0.33
0.38
Piont III
2.44
2.09
0.17
0.76
CCD, cts
rel, 1/cm
(c)
Point II
Point III
Point I
100 μm
28.8 HV
31.8 HV
50 μm
Piont I
0.37
0.69
0.29
0.26
Piont II
0.20
1.38
0.37
0.11
Piont III
3.62
4.07
1.07
1.18
CCD, cts
rel, 1/cm
(d)
Point II
Point III
Point I
100 μm
22.5 HV
27.6 HV
50 μm
Piont I
0.53
0.22
0.15
0.12
Piont II
0.56
1.90
0.24
0.28
Piont III
7.1
3.47
0.51
0.98
CCD, cts
rel, 1/cm

1. Download: Download high-res image (2MB)
2. Download: Download full-size image

Fig. 10. Microhardness and phase distribution at different positions of the cross-sectional rust layer of 3Ni-0.5Mo steel after different corrosion durations (α: α-FeOOH, β: β-FeOOH, γ: γ-FeOOH, M: Fe_3O_4, H: Fe_2O_3): (a) 96 h, (b) 192 h, (c) 384 h, and (d) 768 h.

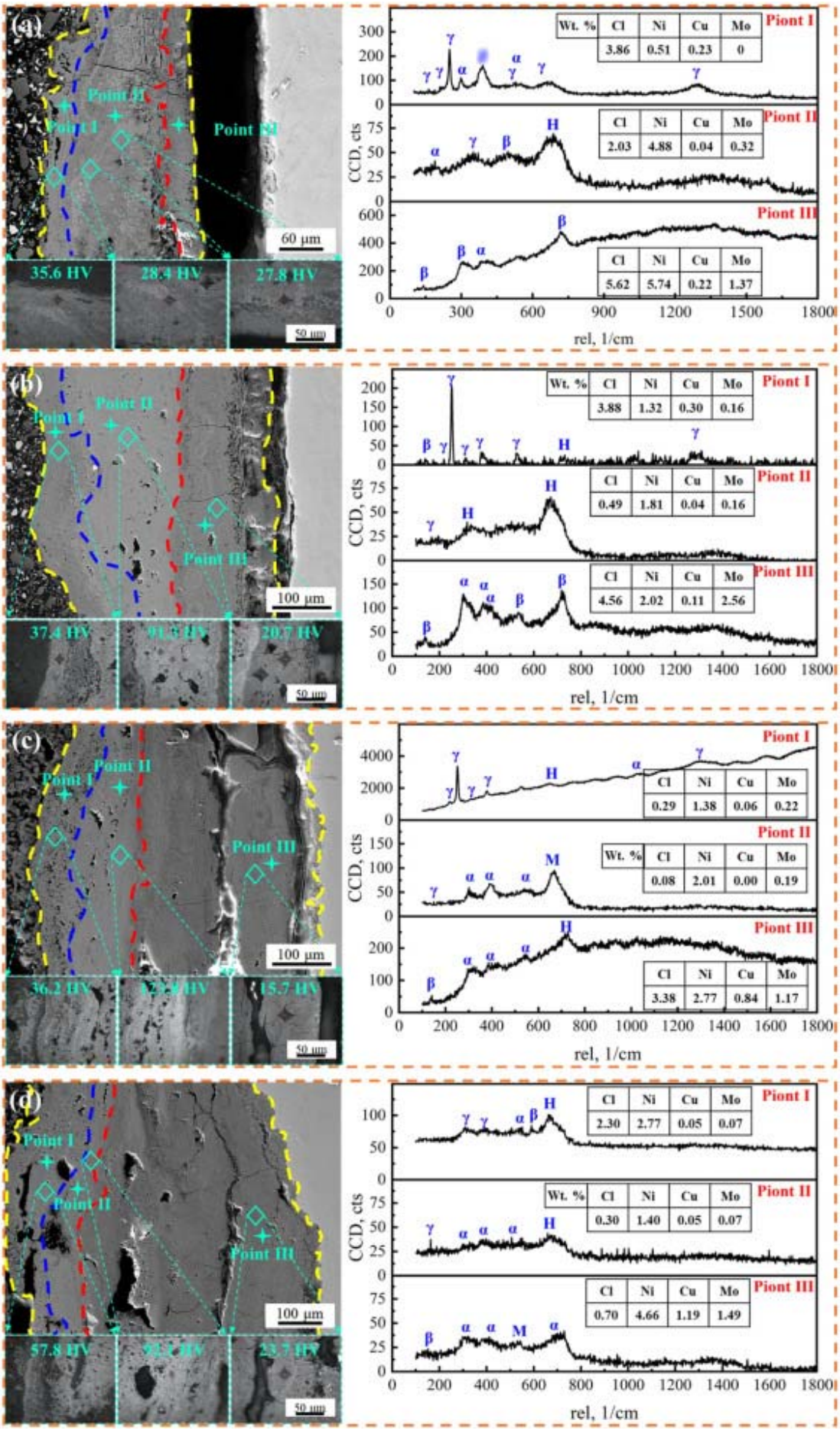
(a)
Point I
Point II
Point III
60 μm
35.6 HV
28.4 HV
27.8 HV
50 μm
Wt. %
Cl
Ni
Cu
Mo
Piont I
3.86
0.51
0.23
0
Piont II
2.03
4.88
0.04
0.32
Piont III
5.62
5.74
0.22
1.37
CCD, cts
rel, 1/cm
(b)
Point I
Point II
Point III
100 μm
37.4 HV
91.5 HV
20.7 HV
50 μm
Piont I
3.88
1.32
0.30
0.16
Piont II
0.49
1.81
0.04
0.16
Piont III
4.56
2.02
0.11
2.56
CCD, cts
rel, 1/cm
(c)
Point I
Point II
Point III
100 μm
36.2 HV
15.7 HV
50 μm
Piont I
0.29
1.38
0.06
0.22
Piont II
0.08
2.01
0.00
0.19
Piont III
3.38
2.77
0.84
1.17
CCD, cts
rel, 1/cm
(d)
Point I
Point II
Point III
100 μm
57.8 HV
23.7 HV
50 μm
Piont I
2.30
2.77
0.05
0.07
Piont II
0.30
1.40
0.05
0.07
Piont III
0.70
4.66
1.19
1.49
CCD, cts
rel, 1/cm

1. Download: Download high-res image (2MB)
2. Download: Download full-size image

Fig. 11. Microhardness and phase distribution at different positions of the cross-sectional rust layer of 3Ni-1Mo steel after different corrosion durations: (a) 96 h, (b) 192 h, (c) 384 h, and (d) 768 h.

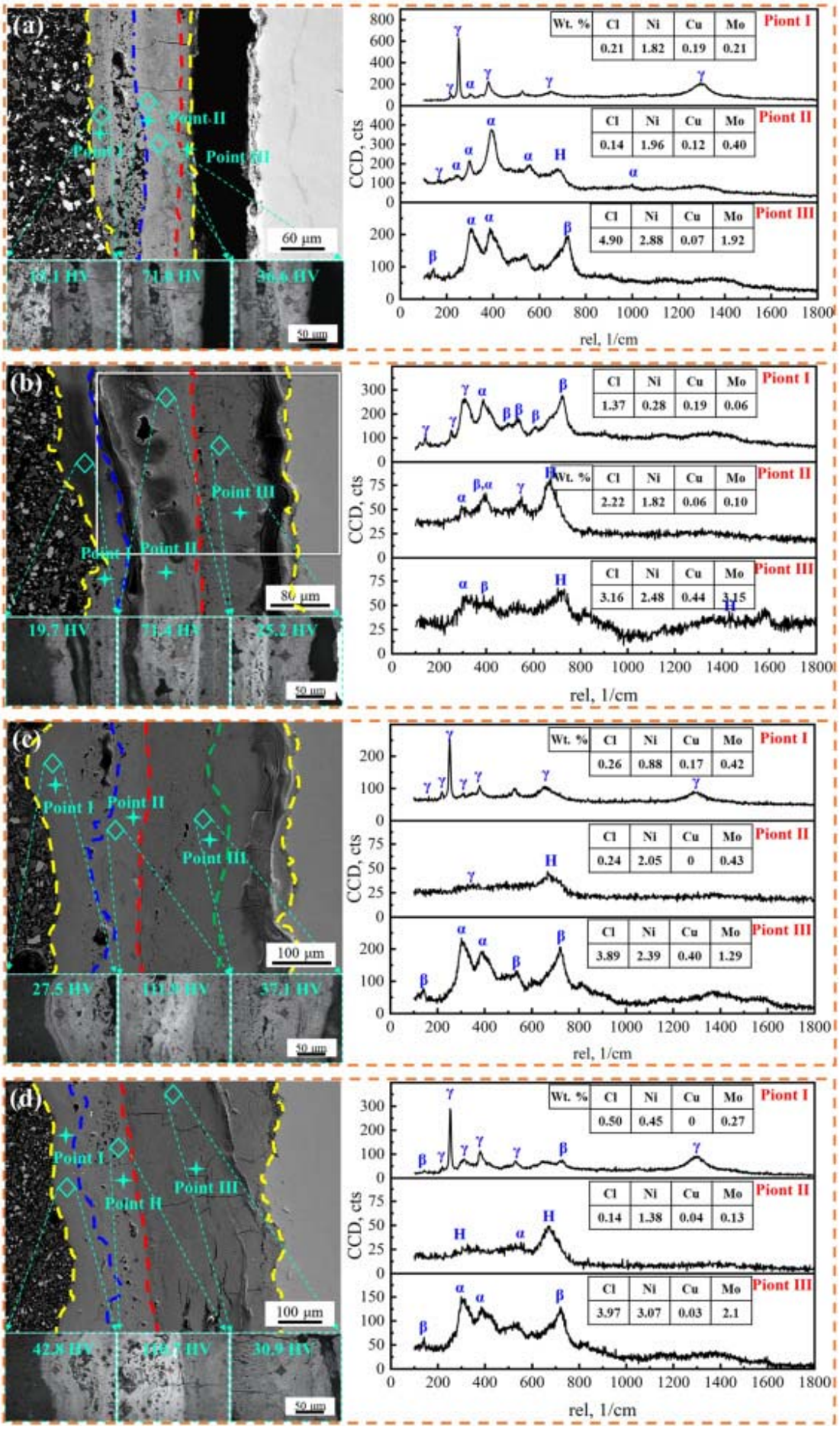
(a)
Point I
Point II
Point III
60 μm
50 μm
(b)
Point I
Point II
Point III
80 μm
19.7 HV
50 μm
(c)
Point I
Point II
Point III
100 μm
27.5 HV
50 μm
(d)
Point I
Point II
Point III
100 μm
42.8 HV
50 μm
Wt. % Cl Ni Cu Mo
Piont I
0.21 1.82 0.19 0.21
Piont II
0.14 1.96 0.12 0.40
Piont III
4.90 2.88 0.07 1.92
Piont I
1.37 0.28 0.19 0.06
Piont II
2.22 1.82 0.06 0.10
Piont III
3.16 2.48 0.44 3.15
Piont I
0.26 0.88 0.17 0.42
Piont II
0.24 2.05 0 0.43
Piont III
3.89 2.39 0.40 1.29
Piont I
0.50 0.45 0 0.27
Piont II
0.14 1.38 0.04 0.13
Piont III
3.97 3.07 0.03 2.1
CCD, cts
rel, 1/cm

1. Download: Download high-res image (2MB)
2. Download: Download full-size image

Fig. 12. Microhardness and phase distribution at different positions of the cross-sectional rust layer of 3Ni-1.5Mo steel after different corrosion durations: (a) 96 h, (b) 192 h, (c) 384 h, and (d) 768 h.

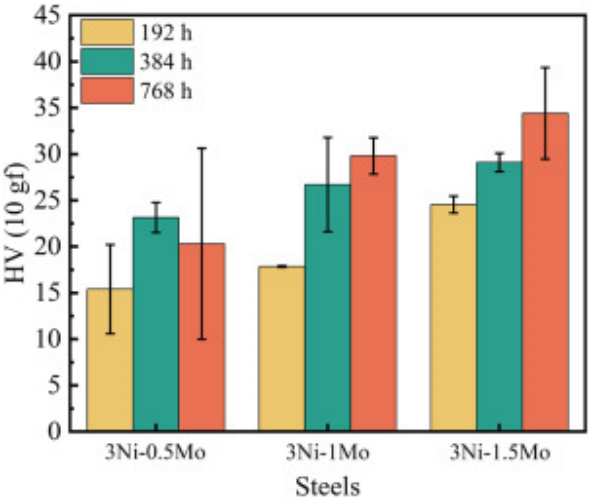

1. Download: Download high-res image (137KB)
2. Download: Download full-size image

Fig. 13. Microhardness statistics of Layer C of the prepared steels after different corrosion cycles.

The localized Cl element enrichment within the rust layer tends to align with distinct phase peaks of β-FeOOH, discernible at positions such as Point I and Point II in Fig. 10(a), as well as Point III in Fig. 10(d). As prior investigations have outlined [57], the mass fraction of Cl element in β-FeOOH typically ranges from 2 % to 7 %. Consequently, the prevailing manifestation of Cl within the rust layer of the experimental steels in this study is predominantly in the form of β-FeOOH. The presence of β-FeOOH also rationalizes the occurrence of minor microcracks and the relatively subdued microhardness values detected within Layer C. In more specific terms, the generation of β-FeOOH involves a multifaceted transformation process, proceeding as follows: $FeCl_2 \rightarrow$ β-$Fe_2(OH)_3Cl \rightarrow$ GR1(Cl^-) → β-FeOOH [54]. Importantly, owing to its relatively lower density (3.0 g cm^{-3}), the associated volume changes that arise upon its formation can potentially disrupt the structural integrity of the rust layer. Given that Layer C houses a significant proportion of β-FeOOH, the occurrence of microcracks theoretically could compromise the structural integrity of the rust layer, consequently affecting its protective efficacy. Conversely, an intriguing phenomenon occurs in Layer C where the microhardness values markedly increase over prolonged corrosion periods (as depicted in Fig. 13). This trend is particularly pronounced in the 3Ni-1Mo and 3Ni-1.5Mo steels. This observation proposes the possibility of a synergistic chemical interaction between Mo and Ni that effectively offsets the adverse impact of volume contraction. Even more noteworthy is that the microhardness of Layer C also exhibits a positive correlation with the Mo content, as similarly indicated in Fig. 13. These research findings provide robust support for the proposition that Mo contributes to the increased compactness of Layer C, consequently

heightening the corrosion resistance of rust layer. As Layer C predominantly comprises α-FeOOH and β-FeOOH, the improvement in the corrosion resistance of 3Ni steels by Mo may be reflected in the enhancement of both the morphology and content of α-FeOOH and β-FeOOH within Layer C and attributed to the formation of an alkaline steel-rust interface. These intricate dynamics will be meticulously examined in forthcoming sections.

4.3. The effect of Mo on corrosion thermodynamics of matrix and nanoscale FeOOH in corrosion products

The surface electron work function serves as a physical parameter that elucidates the corrosion propensity of different crystal planes. It represents the minimal thermodynamic work demanded for an electron to disengage from the solid surface into the vacuum. This property hinges on the electronic structure and crystallinity of two to three atomic layers of the surface. A lower surface work function corresponds to heightened electron activity and impaired resistance to corrosion [58], [59], [60]. To explore the particulars, the equilibrium lattice constants of the [Fe] unit cell underwent optimization via a 12 × 12 × 12 Monkhorst-Pack k-point grid, employing $a = b = c = 1$ Å for Brillouin zone sampling. Utilizing these lattice constants, a Fe(110) plane comprising 5 atomic layers was fabricated, encompassing 80 Fe atoms. To account for the impact of doping, Ni and Mo atoms were introduced onto the Fe(110) plane, as illustrated in Fig. 14(a). These planes were spaced apart by a 15 Å vacuum layer in the *z*-direction. During the structural optimization of this model, a 4 × 4 × 1 k-point grid at the central gamma point was employed. All atomic layers were permitted to undergo complete relaxation. The outcomes stemming from first-principles calculations grounded in density functional theory (depicted in Fig. 14(b, c)) unveiled that the surface work function of the 3Ni steel progressed from 4.82 to 4.86 eV post-Mo doping. Hence, the thermodynamic outcome of the electron work function for the substrate aligns with the kinetic results demonstrated by electrochemistry, as evidenced by previous Tafel fitting. This concurrence points towards the assertion that the inclusion of Mo serves to enhance the corrosion resistance of the substrate surface.

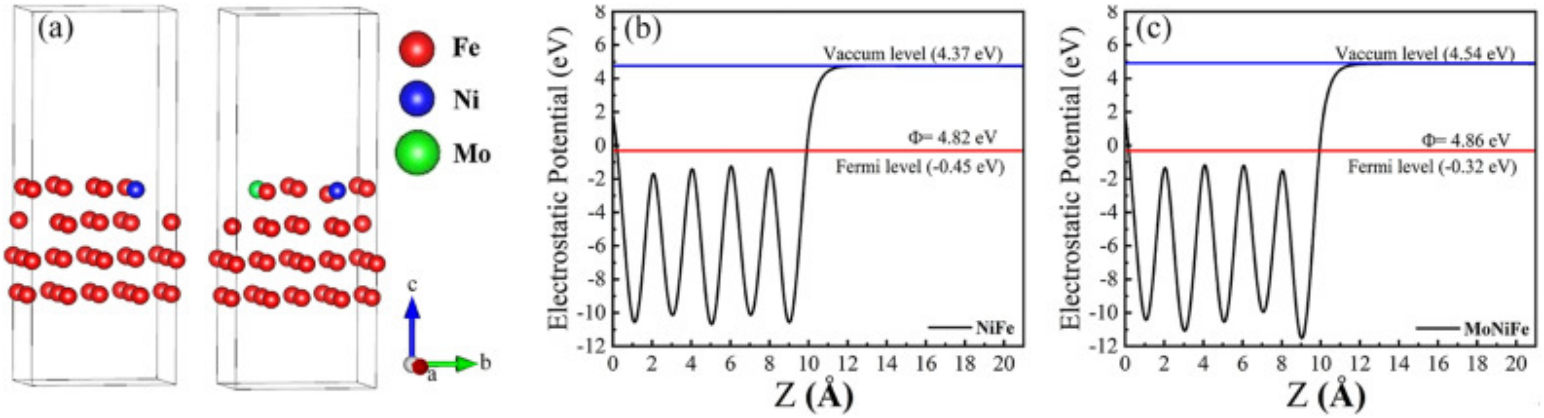

1. Download: Download high-res image (343KB)

2. Download: Download full-size image

Fig. 14. (a) Surface structure model of Fe after element doping and (b, c) surface work function calculation results.

In order to gain a deeper understanding of the influence of Mo on the corrosion products and the corrosion mechanism of the 3Ni series weathering steel, a nanoscale investigation was carried out on the rust layers of the three experimental steels post 768 h of corrosion. The TEM morphologies, corresponding HRTEM images, and the selected area diffraction pattern (SADP) of the corrosion products are presented in Fig. 15, Fig. 16, Fig. 17. Across all three experimental steels, the corrosion products encompass α-FeOOH, γ-FeOOH, β-FeOOH, Fe_3O_4, NiO, and MoO_2/MoO_3, thus corroborating the XPS detection outcomes. The corrosion products exhibit cluster formations, composed of spherical particles with dimensions ranging from 5 to 20 nm. Previous research [38,39] has suggested that Mo can facilitate the formation generation of NiO, demonstrating a certain degree of synergistic interaction between them. In this investigation, as the Mo content increases, Fe_3O_4 undergoes a refinement. The size of Fe_3O_4 decreases from 400 nm × 800 nm in the 3Ni-0.5Mo steel to 200 nm × 400 nm in the 3Ni-1.5Mo steel. This trend is evident in Region B of Fig. 15, Region C of Fig. 16, and Region C of Fig. 17. Simultaneously, Mo has a significant impact on increasing the Ni content within rust particles. This phenomenon is visible in Fig. 17, where both Regions A and C comprise Fe_3O_4. Nevertheless, Region A records higher Mo and Ni element concentrations, which lead to a comparatively reduced size of Fe_3O_4 particles. Additionally, the dimensions of α-FeOOH and β-FeOOH also witness a reduction alongside the increasing of Mo and Ni element contents, as observed in Regions A and C of Fig. 16. This implies that the synergistic interaction between Mo and Ni can refine the size of corrosion products, which is crucial for the formation of a more compact rust layer.

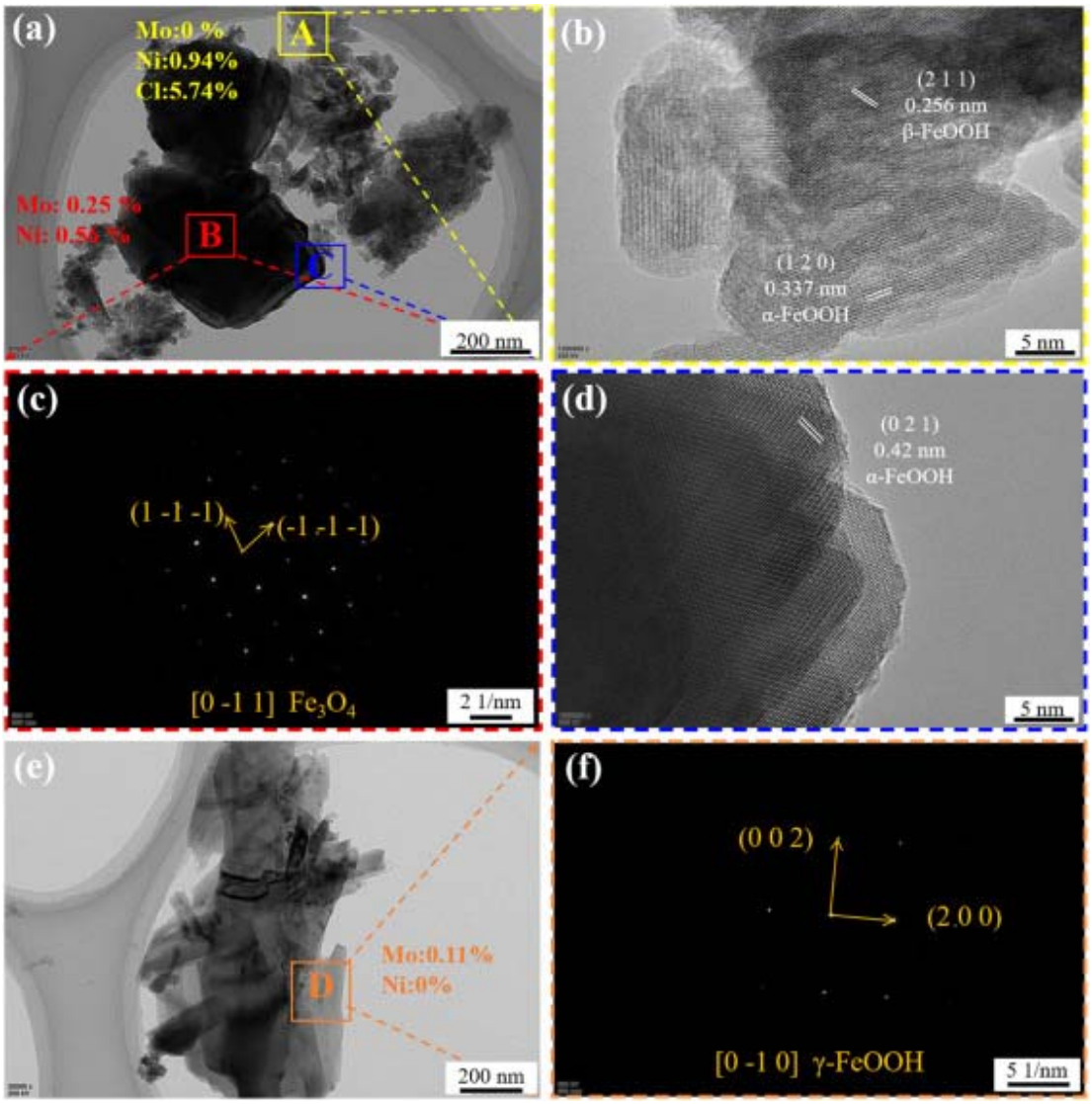

1. Download: Download high-res image (1MB)
2. Download: Download full-size image

Fig. 15. TEM morphologies of the rust particles of 3Ni-0.5Mo steel after corrosion for 768 h: (a, e) morphology of the rust particles, (b) HRTEM image of Region A, (c) SADP of Region B, (d) HRTEM image of Region C, and (f) SADP of Region D.

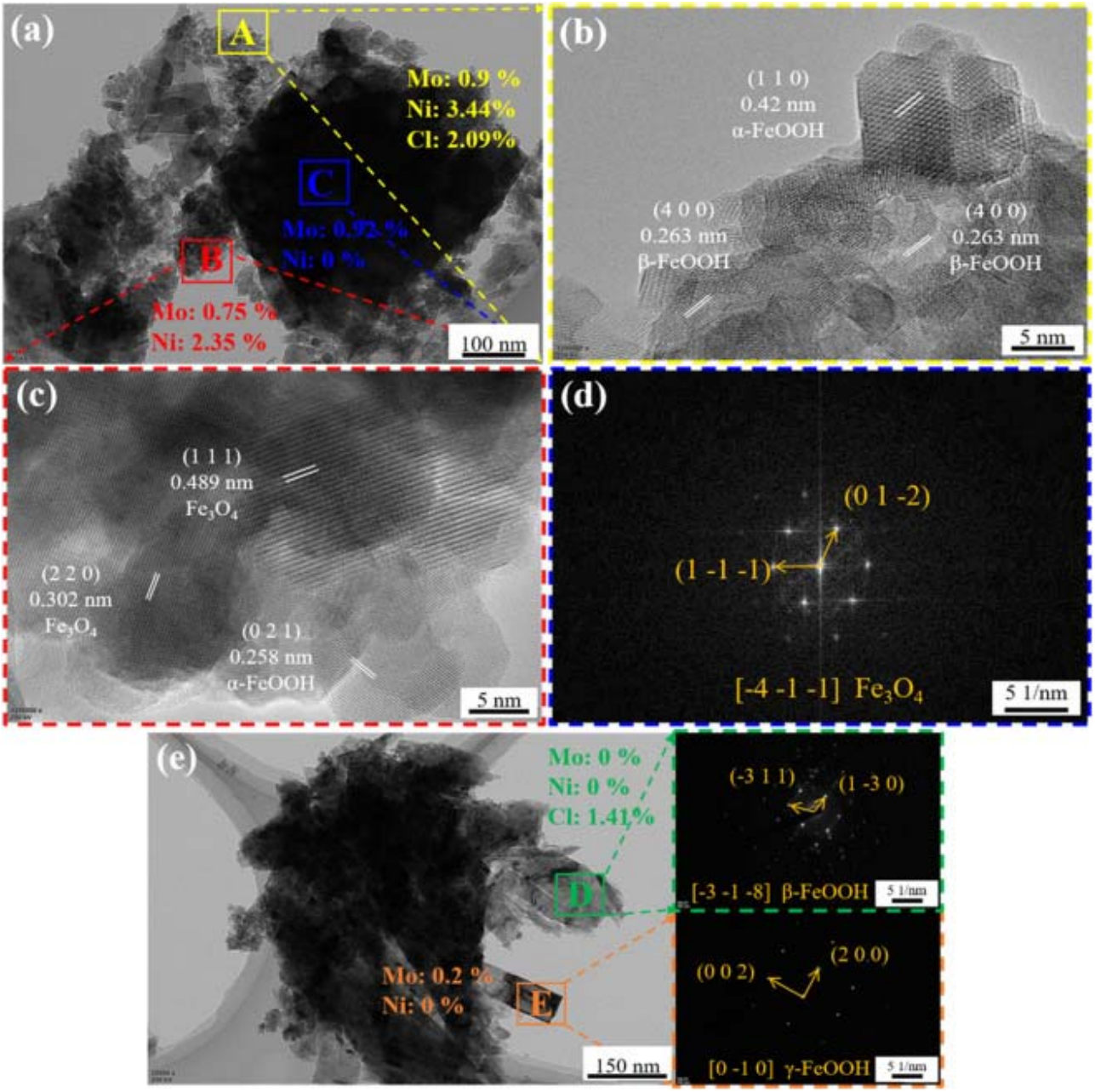

1. Download: Download high-res image (1MB)
2. Download: Download full-size image

Fig. 16. TEM morphologies of the rust particles of 3Ni-1Mo steel after corrosion for 768 h: (a, e) morphology of the rust particles, (b) HRTEM image of Region A, (c) SADP of Region B, and (d) HRTEM image of Region C.

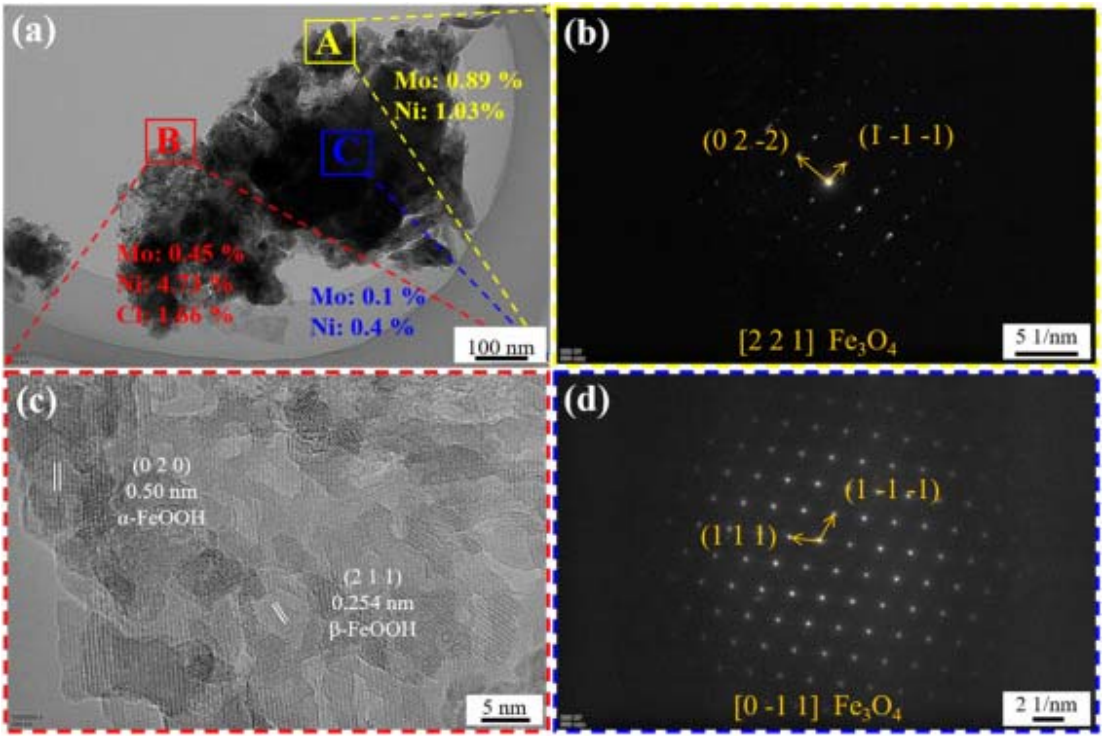

1. Download: Download high-res image (776KB)
2. Download: Download full-size image

Fig. 17. TEM morphologies of the rust particles of 3Ni-1.5Mo steel after corrosion for 768 h: (a) morphology of the rust particles, (b) SADP of Region A, (c) HRTEM image of Region B, and (d) SADP of Region C.

As the rust layer develops on the matrix, it involves a complex interplay of corrosion products that goes beyond the mere formation of iron hydroxides and oxides. This includes the generation and transformation of corrosion products involving Ni and Mo. These intricate processes are represented by various chemical reaction equations, some of which are outlined below [61,24]:

$$2Ni + O_2 + 2H_2O \rightarrow 2Ni(OH)_2 \quad (3)$$

$$Ni(OH)_2 \rightarrow NiO + H_2O \quad (4)$$

$$2Fe(OH)_2 + Ni(OH)_2 \rightarrow NiFe_2O_4 + 2H_2O \quad (5)$$

$$Mo + 2H_2O + O_2 \rightarrow Mo(OH)_4 \quad (6)$$

$$Mo(OH)_4 + H_2O + \frac{1}{2}O_2 \rightarrow Mo(OH)_6 \quad (7)$$

$$Mo(OH)_4 \rightarrow MoO_2 + 2H_2O \quad (8)$$

$$Mo(OH)_6 \rightarrow MoO_3 + 3H_2O \quad (9)$$

The oxidation of Mo and Ni results in the formation of MoO_2, MoO_3, NiO, and $NiFe_2O_4$. These oxides serve as nucleation sites for corrosion products such as FeOOH, promoting both the refinement and aggregation of rust particles, thereby enhancing the compactness of corrosion products (as elucidated in Fig. 15, Fig. 16, Fig. 17). The HRTEM images of corrosion products reveal that α-FeOOH and β-FeOOH coexist in most cases, both of which are nano-scale compounds, as demonstrated in Figs. 15(b), 16(b), and 17(c). This visual evidence further supports the previous hypothesis that Layer C primarily consists of a combination of α-FeOOH and β-FeOOH. Moreover, the synthesis of evidence from HRTEM and microhardness findings strengthens the proposition that Mo and Ni, through their mutually synergistic chemical reactions, work together to promote the formation of nanoscale FeOOH, thus fortifying the compactness of Layer C.

4.4. The formation mechanism of the stable rust layer with a three-layer structure

The above research findings highlighted the exceptional corrosion resistance exhibited by 3Ni-Mo weathering steel in simulated high-salt and high-humidity marine atmospheric corrosion environments. The intricate corrosion mechanism and the evolution of rust layers are illustrated in Fig. 18. During the initial stages of corrosion, a notable portion of Fe undergoes dissolution, yielding Fe^{2+} ions, some of which further oxidize to Fe^{3+} ions. Consequently, the emergence of primary corrosion products γ-FeOOH and Fe_3O_4 transpires, establishing Layer A and Layer B. However, at this point, a stable rust layer has not yet formed, and the adhesion between the rust layer and the substrate is relatively weak. Layer B, primarily consisting of Fe_2O_3/Fe_3O_4, also contains a significant amount of $NiFe_2O_4$ (where Ni^{2+} replaces Fe^{2+} in Fe_3O_4). This imparts electronegativity to the layer, enabling it to repel Cl^-. As the corrosion process continues, both γ-FeOOH and Fe_3O_4 undergo further transformation into the more stable α-FeOOH, leading to a

significant reduction in the concentration of Fe^{2+} within the rust layer. At this stage, the rust layer undergoes a transition towards a more stable three-layer structure. resulting in a substantial decrease in the corrosion rate. The reduction in corrosion rate does not impede the shift from γ-FeOOH/Fe_3O_4 to α-FeOOH. Consequently, the expansion of Layer C ensues. However, before Layer B can effectively insulate Cl^-, Cl^- can infiltrate the rust layer, reaching both Layer C and the substrate surface. In an environment characterized by heightened Cl^- concentration and acidic conditions, the synergistic impact of high Cl^- fosters the substantial formation of β-FeOOH in Layer C. This elevated Cl^- concentration expedites corrosion through autocatalytic mechanisms, instigating acidification of the steel-rust layer interface. Once Layer B can effectively shield against Cl^-, the presence of Cl^- becomes confined within Layer C, existing not as ions but in the form of β-FeOOH. Ultimately, Layer C, composed of both α-FeOOH and β-FeOOH, becomes the predominant part of the rust layer.

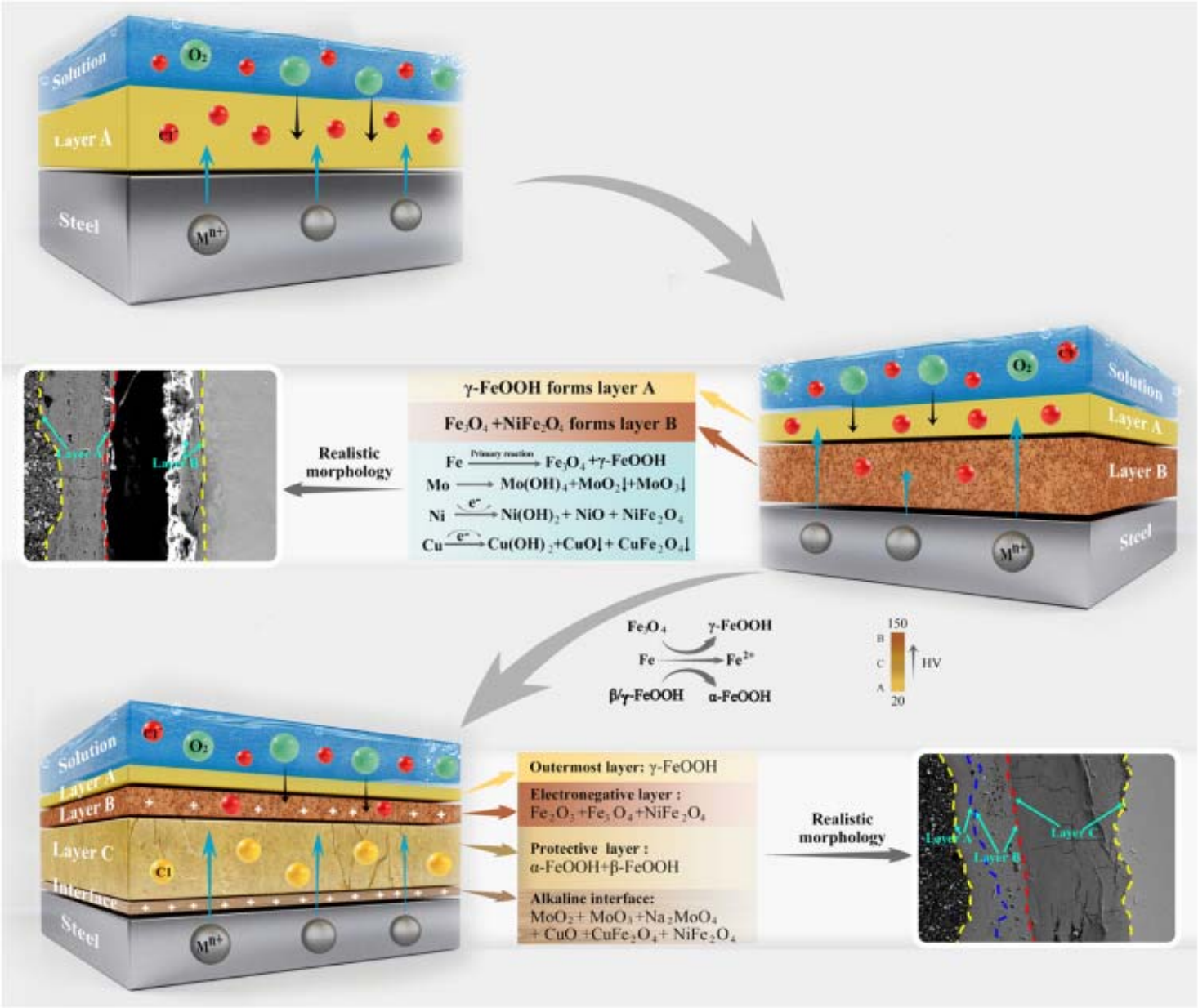

1. Download: Download high-res image (1MB)
2. Download: Download full-size image

Fig. 18. Schematic diagram of corrosion resistance mechanism and rust layer evolution of 3Ni-Mo weathering steel in a simulated marine atmospheric environment.

As Fe undergoes oxidation, alloying elements like Ni, Cu, and Mo also dissolve, generating metal cations. Initially, these cations combine with OH^- ions produced at the cathode, leading to the formation of hydroxides. These hydroxides then undergo further transformation into metal oxides. Since $Ni(OH)_2$ is soluble in water, Ni^{2+} ion is distributed throughout the entire growing rust layer. A portion of Ni^{2+} replaces Fe^{2+} in Fe_3O_4, resulting in the formation of $NiFe_2O_4$, while another part undergoes dehydration to yield

NiO [39], [40], [41]. The hydroxides of Cu similarly transition into CuO, accumulating at the steel-rust interface. Certain Cu^{2+}, akin to Ni^{2+}, take on the role of Fe^{2+} in Fe_3O_4, engendering electronegative $CuFe_2O_4$ [40]. The hydroxides of Mo will further transform into MoO_2, typically precipitating within corrosion pits and reducing local corrosion rates. Under acidic conditions, MoO_2 conveniently transforms into MoO_3, ultimately yielding insoluble molybdate, contributing to substantial Mo accumulation at the steel-rust interface. The deposition of these insoluble Cu and Mo oxides limits the number of active dissolution sites and fills cracks and imperfections, thereby reducing the overall corrosion rate. The increased enrichment of $CuFe_2O_4$ at the steel-rust interface enhances electronegativity, exceeding that of Layer B. This hinders interface acidification and the localized accelerated corrosion prompted by Cl^-. Simultaneously, it fosters the development of an alkaline steel-rust interface. Moreover, the combined effects of MoO_2, MoO_3, and NiO refine the nano-sized α-FeOOH and β-FeOOH constituents within Layer C, enhancing both the compactness and the protective characteristics of the rust layer. At this stage, a stable rust layer marked by a complete three-layer structure and an alkaline steel-rust interface is fully established.

The synergistic combination of the dual Cl^- exclusion mechanism, which operates in both Layer B and alkaline steel-rust interface, presents a robust resistance to Cl^-, effectively establishing a dual barrier against its intrusion. Simultaneously, Cl^- is sequestered within Layer C in the form of β-FeOOH, making it challenging to freely diffuse. In addition, the joint refining effects of Mo and Ni on the corrosion products within Layer C, coupled with the protective role of stable α-FeOOH, compensate for the corrosion resistance issues caused by cracking of the rust layer induced by β-FeOOH. This unique stable rust layer, along with the alkaline steel-rust interface, makes it possible for the 3Ni-Mo advanced weathering steel to be applied without coatings in environments characterized by high humidity and salt exposure, highlighting its feasibility in conditions featuring elevated humidity, high temperatures, and even exposure to salt spray.

5. Conclusions

1) The enhancement in the protective properties of the rust layer is directly associated with the increase in Mo content, ranging from 0.5 to 1.5 wt.%. This advancement is particularly evident in the reduced corrosion rate of 3Ni-Mo steel, decreasing from 1.74 to 1.31 mm y^{-1} after 768 h of corrosion. Moreover, the heightened Mo content plays a pivotal role in expediting the formation of a stable rust layer and augmenting the proportion of α-FeOOH within this protective layer.
2) The rust layer developed on the 3Ni-Mo weathering steel exhibits a well-defined three-layer structure. The outer layer primarily consists of γ-FeOOH, the intermediate layer is mainly composed of Fe_2O_3/Fe_3O_4, and the inner layer constitutes the predominant portion of the rust layer and is primarily composed of α-FeOOH and β-FeOOH. An alkaline interface enriched with $NiFe_2O_4$ and $CuFe_2O_4$ forms between the innermost layer and the substrate, exhibiting higher electronegativity and effectively preventing Cl^--induced interface acidification and pitting corrosion. Additionally, the higher Mo content expedites the formation of the alkaline interface and promotes the densification of the innermost layer.
3) Mo significantly bolsters the corrosion resistance of 3Ni steel through a series of mechanisms that collectively fortify its resilience in corrosive environments: (i) Deposition of MoO_2, MoO_3, and molybdate on both the innermost layer and alkaline steel-rust interface, repairing corrosion pits and fills cracks; (ii) Facilitates the generation of compounds such as $NiFe_2O_4$ and $CuFe_2O_4$, heightening the electronegativity of the intermediate rust layer and the steel-rust interface; (iii) Mo creates extra nucleation sites for hydroxide oxides through oxide formation, leading to the development of nano-sized α-FeOOH and β-FeOOH within the inner layer. This strengthens the stability and compactness of the inner layer.

Declaration of competing interest

We wish to confirm that there are no known conflicts of interest associated with this publication and there has been no significant financial support for this work that could have influenced its outcome.

Acknowledgments

Gang Niu, Xiaojia Yang, Kun Li, and Huibin Wu appreciate the support from the National Key R&D Program of China (No. 2021YFB3701700). Gang Niu appreciates the support from the National Natural Science Foundation of China (No. 52304389). Gang Niu and Huibin Wu appreciate the support from the Fundamental Research Funds for the Central Universities (No. FRF-BD-23-01). Gang Niu appreciates the support from the China Postdoctoral Science Foundation (No. 2022M720402). Na Gong appreciates the support from the Structural Metal Alloy Program (SMAP), Grant No. A18B1b0061, and Manufacturing of Multi-Material Net-Shape Parts with Heterogeneous Properties (MMNH), Grant no. M22K5a0045 in A*STAR.

Appendix. Supplementary materials

Download: Download Word document (12MB)

References

[1]

I. Díaz, H. Cano, P. Lopesino, D. de la Fuente, B. Chico, J.A. Jiménez, S.F. Medina, M. Morcillo

Corros. Sci., 141 (2018), pp. 146-157

View PDFView articleView in ScopusGoogle Scholar

[2]

X. Yang, Y. Yang, M. Sun, J. Jia, X. Cheng, Z. Pei, Q. Li, D. Xu, K. Xiao, X. Li

J. Mater. Sci. Technol., 104 (2022), pp. 67-80

View PDFView articleGoogle Scholar

[3]

J. Peng, B. Chen, Z. Wang, J. Guo, B. Wu, S. Hao, Q. Zhang, L. Gu, Q. Zhou, Z. Liu, S. Hong, S. You, A. Fu, Z. Shi, H. Xie, D. Cao, C.J. Lin, G. Fu, L.S. Zheng, Y. Jiang, N. Zheng

Nature, 586 (2020), pp. 390-394

CrossrefView in ScopusGoogle Scholar

[4]

X. Li, D. Zhang, Z. Liu, Z. Li, C. Du, C. Dong

Nature, 527 (2015), pp. 441-442

CrossrefView in ScopusGoogle Scholar

[5]

P. Liu, Q. Zhang, X. Li, J. Hu, F. Cao

J. Mater. Sci. Technol., 64 (2021), pp. 99-113

View PDFView articleView in ScopusGoogle Scholar

[6]

Y. Wang, J. Li, L. Zhang, L. Zhang, Q. Wang, T. Wang

Corros. Sci., 177 (2020), Article 108997

View PDFView articleView in ScopusGoogle Scholar
[7]

C. Comas, F. Huet, K. Ngo, M. Fregonese, H. Idrissi, B. Normand

Corros. Sci., 193 (2021), Article 109885

View PDFView articleView in ScopusGoogle Scholar
[8]

C. Yang, Y. Luan, D. Li, Y. Li

J. Mater. Sci. Technol., 35 (2019), pp. 1298-1308

View PDFView articleView in ScopusGoogle Scholar
[9]

A. Usami, H. Kihira, T. Kusunoki, S. Giho

3 % Ni-Weathering Steel Plate for Uncoated Bridges at High Air-Bone Salt Environments

Nippon Steel Technical Report (2002)

Google Scholar
[10]

M. Kimura, H. Kihira, N. Ohta, M. Hashimoto, T. Senuma

Corros. Sci., 47 (2005), pp. 2499-2509

View PDFView articleView in ScopusGoogle Scholar
[11]

W. Wu, Z. Dai, Z. Liu, C. Liu, X. Li

Corros. Sci., 183 (2021), Article 109353

View PDFView articleGoogle Scholar
[12]

J. Jia, Z. Liu, X. Cheng, C. Du, X. Li

Corros. Commun., 2 (2021), pp. 82-90

View PDFView articleView in ScopusGoogle Scholar
[13]

X. Yang, J. Jia, X. Li, Q. Li, Z. Sun, C. Du, X. Li

Constr. Build. Mater., 408 (2023), Article 133820

View PDFView articleView in ScopusGoogle Scholar
[14]

Y. Fan, W. Liu, Z. Sun, T. Chowwanonthapunya, Y. Zhao, B. Dong, T. Zha ng, W. Banthukul

Constr. Build. Mater., 266 (2021), Article 120937

View PDFView articleView in ScopusGoogle Scholar
[15]

M. Morcillo, I. Díaz, H. Cano, B. Chico, D. de la Fuente

Constr. Build. Mater., 222 (2019), pp. 750-765

View PDFView articleView in ScopusGoogle Scholar
[16]

X.Q. Cheng, Y.W. Tian, X.G. Li, C. Zhou

Mater. Corros., 65 (2014), pp. 1033-1037

CrossrefView in ScopusGoogle Scholar
[17]

W. Wu, X. Cheng, J. Zhao, X. Li

Corros. Sci., 165 (2020), Article 108416

View PDFView articleView in ScopusGoogle Scholar
[18]

I. Diaz, H. Cano, D. de la Fuente, B. Chico, J.M. Vega, M. Morcillo

Corros. Sci., 76 (2013), pp. 348-360

View PDFView articleView in ScopusGoogle Scholar
[19]

M. Morcillo, I. Díaz, B. Chico, H. Cano, D. de la Fuente

Corros. Sci., 83 (2014), pp. 6-31

View PDFView articleView in ScopusGoogle Scholar
[20]

G. Niu, R. Yuan, R.D.K. Misra, N. Gong, Z.-H. Zhang, H.-X. Chen, H.-B. Wu, C.-J. Shang, X.-P. Mao

Acta Metall. Sin.-Engl. Lett., 37 (2023), pp. 1-17

Google Scholar
[21]

Y. Ma, Y. Li, F. Wang

Mater. Chem. Phys., 112 (2008), pp. 844-852

View PDFView articleView in ScopusGoogle Scholar
[22]

P. Klomjit, M. Omoda, D. Mizuno, N. Ishikawa, N. Palsson, W. Pongsaksawad, E. Viyanit

Corrosion, 75 (2019), pp. 960-972

CrossrefView in ScopusGoogle Scholar
[23]

T. Nishimura

Sci. Technol. Adv. Mater., 9 (2008), Article 013005

CrossrefView in ScopusGoogle Scholar
[24]

Y. Fan, W. Liu, S. Li, T. Chowwanonthapunya, B. Wongpat, Y. Zhao, B. Dong, T. Zhang, X. Li

J. Mater. Sci. Technol., 39 (2020), pp. 190-199

View PDFView articleView in ScopusGoogle Scholar
[25]

X. Cheng, Z. Jin, M. Liu, X. Li

Corros. Sci., 115 (2017), pp. 135-142

View PDFView articleCrossrefGoogle Scholar
[26]

C.P. Larrabee, S.K. Coburn

Proceedings to the First International Congress on Metallic Corrosion, Butterworths, London (1962)

Google Scholar
[27]

S. Unjoh, S. Nakatani, K.-I. Tamura, J. Fukui, J.-I. Hoshikuma

Japanese Seismic Design Specifications for Highway Bridges, Nist Special Publication (2002), pp. 231-240

https://doi.org/10.1142/9789812704252_0014
Google Scholar
[28]

E.K.D. Benito, A. Ueno, T. Fukuyama

J. Adv. Concr. Technol., 20 (2022), pp. 313-327

CrossrefView in ScopusGoogle Scholar
[29]

M. Sun, X. Yang, C. Du, Z. Liu, Y. Li, Y. Wu, H. San, X. Su, X. Li

J. Mater. Sci. Technol., 81 (2021), pp. 175-189

View PDFView articleView in ScopusGoogle Scholar
[30]

Y. Yang, T. Zhang, Y. Shao, G. Meng, F. Wang

Corros. Sci., 73 (2013), pp. 250-261

View PDFView articleView in ScopusGoogle Scholar
[31]

D. Song, J. Hao, F. Yang, H. Chen, N. Liang, Y. Wu, J. Zhang, H. Ma, E.E . Klu, B. Gao, Y. Qiao, J. Sun, J. Jiang

J. Alloy. Compd., 809 (2019), Article 151787

View PDFView articleView in ScopusGoogle Scholar
[32]

X. Hao, J. Dong, X. Mu, J. Wei, C. Wang, W. Ke

J. Mater. Sci. Technol., 35 (2019), pp. 799-811

View PDFView articleView in ScopusGoogle Scholar

[33]

X. Lu, D. Zhang, W. Xu, A. Yu, J. Zhang, M. Tamaddon, J. Zhang, X. Qu, C. Liu, B. Su

Corros. Sci., 177 (2020), Article 109007

View PDFView articleView in ScopusGoogle Scholar
[34]

J.P. Perdew, K. Burke, M. Ernzerhof

Phys. Rev. Lett., 77 (1996), pp. 3865-3868

Google Scholar
[35]

G. Kresse, J. Furthmüller

Phys. Rev. B, 54 (1996), pp. 11169-11186

View in ScopusGoogle Scholar
[36]

G. Kresse, J. Furthmüller

Comp. Mater. Sci., 6 (1996), pp. 15-50

View PDFView articleGoogle Scholar
[37]

G. Kresse, D. Joubert

Phys. Rev. B, 59 (1999), pp. 1758-1775

View in ScopusGoogle Scholar
[38]

P.E. Blöchl

Phys. Rev. B, 50 (1994), pp. 17953-17979

View in ScopusGoogle Scholar
[39]

X. Wei, D. Fu, M. Chen, W. Wu, D. Wu, C. Liu

J. Mater. Sci. Technol., 64 (2021), pp. 222-232

View PDFView articleView in ScopusGoogle Scholar
[40]

B. Dong, W. Liu, L. Chen, T. Zhang, Y. Fan, Y. Zhao, H. Li, W. Yang, Y. S un

Corros. Sci., 209 (2022), Article 110741

View PDFView articleView in ScopusGoogle Scholar
[41]

M. Sun, Y. Pang, C. Du, X. Li, Y. Wu

Constr. Build. Mater., 302 (2021), Article 124346

View PDFView articleView in ScopusGoogle Scholar
[42]

H.J. Flitt, D.P. Schweinsberg

Corros. Sci., 47 (2005), pp. 3034-3052

View PDFView articleView in ScopusGoogle Scholar
[43]

Z. Liu, X. Lian, T. Liu, Y. Yang, J. Zhu, H. Dong

Mater. Corros., 71 (2020), pp. 258-266

CrossrefView in ScopusGoogle Scholar
[44]

H. Wang, Y. Song, J. Yu, D. Shan, H. Han

J. Electrochem. Soc., 164 (2017), p. C574

CrossrefView in ScopusGoogle Scholar
[45]

C. Thee, L. Hao, J. Dong, X. Mu, X. Wei, X. Li, W. Ke

Corros. Sci., 78 (2014), pp. 130-137

View PDFView articleView in ScopusGoogle Scholar
[46]

Z. Wang, J. Liu, L. Wu, R. Han, Y. Sun

Corros. Sci., 67 (2013), pp. 1-10

View PDFView articleGoogle Scholar
[47]

S. Huang, W. Wu, Y. Su, L. Qiao, Y. Yan

Corros. Sci., 178 (2021), Article 109071

View PDFView articleView in ScopusGoogle Scholar
[48]

M. Morcillo, B. Chico, I. Díaz, H. Cano, D. de la Fuente

Corros. Sci., 77 (2013), pp. 6-24

View PDFView articleView in ScopusGoogle Scholar
[49]

D. de la Fuente, I. Díaz, J. Simancas, B. Chico, M. Morcillo

Corros. Sci., 53 (2011), pp. 604-617

View PDFView articleView in ScopusGoogle Scholar
[50]

J. Jia, X. Cheng, X. Yang, X. Li, W. Li

Constr. Build. Mater., 259 (2020), Article 119760

View PDFView articleView in ScopusGoogle Scholar
[51]

M. Sun, C. Du, Z. Liu, C. Liu, X. Li, Y. Wu

Corros. Sci., 186 (2021), Article 109427

View PDFView articleView in ScopusGoogle Scholar
[52]

J. Monnier, S. Réguer, E. Foy, D. Testemale, F. Mirambet, M. Saheb, P. D illmann, I. Guillot

Corros. Sci., 78 (2014), pp. 293-303

View PDFView articleView in ScopusGoogle Scholar
[53]

C.R. Hubbard, R.L. Snyder

Powder Diffr., 3 (1988), pp. 74-77

View in ScopusGoogle Scholar
[54]

C. Rémazeilles, P. Refait

Corros. Sci., 49 (2007), pp. 844-857

View PDFView articleView in ScopusGoogle Scholar
[55]

C. Liu, Z. Jiang, J. Zhao, X. Cheng, Z. Liu, D. Zhang, X. Li

Corros. Sci., 166 (2020), Article 108463

View PDFView articleView in ScopusGoogle Scholar
[56]

T. Zhang, Y. Li, X. Li, C. Liu, S. Yang, Z. Yang, X. Li

Corros. Sci., 208 (2022), Article 110708

View PDFView articleView in ScopusGoogle Scholar
[57]

D. Rezel, J.M.R. Genin

Hyperfine Interact., 57 (1990), pp. 2067-2075

View in ScopusGoogle Scholar
[58]

T. Durakiewicz, S. Halas, A. Arko, J.J. Joyce, D.P. Moore

Phys. Rev. B, 64 (2001), Article 045101

Google Scholar
[59]

Y. Shi, L. Collins, R. Feng, C. Zhang, N. Balke, P.K. Liaw, B. Yang

Corros. Sci., 133 (2018), pp. 120-131

View PDFView articleView in ScopusGoogle Scholar
[60]

N. Sathirachinda, R. Pettersson, J. Pan

Corros. Sci., 51 (2009), pp. 1850-1860

[61]

K.Y. Kim, Y.H. Chung, Y.H. Hwang, J.Y. Yoo

Corrosion, 58 (2002), pp. 479-489